Three low-mass companions around aged stars discovered by TESS

Zitao Lin [ORCID],[1][*] Tianjun Gan [ORCID],[1][*] Sharon X. Wang,[1][*] Avi Shporer,[2] Markus Rabus [ORCID],[3] George Zhou,[4] Angelica Psaridi,[5] François Bouchy,[5] Allyson Bieryla,[6] David W. Latham,[3] Shude Mao,[1,7] Keivan G. Stassun [ORCID],[8] Coel Hellier,[9] Steve B. Howell,[10] Carl Ziegler,[11] Douglas A. Caldwell,[10,12] Catherine A. Clark,[13,14] Karen A. Collins [ORCID],[15] Jason L. Curtis,[16] Jacqueline K. Faherty,[17] Crystal L. Gnilka,[10] Samuel K. Grunblatt,[18] Jon M. Jenkins,[10] Marshall C. Johnson,[19] Nicholas Law,[20] Monika Lendl [ORCID],[5] Colin Littlefield,[10,21] Michael B. Lund,[22] Mikkel N. Lund [ORCID],[23] Andrew W. Mann,[20] Scott McDermott,[24] Lokesh Mishra,[5] Dany Mounzer,[5] Martin Paegert,[25] Tyler Pritchard,[26] George R. Ricker,[2] Sara Seager,[2,27,28] Gregor Srdoc,[29] Qinghui Sun,[1] Jiaxin Tang,[1] Stéphane Udry,[5] Roland Vanderspek,[2] David Watanabe,[30] Joshua N. Winn[31] and Jie Yu [ORCID][32]

Affiliations are listed at the end of the paper

ABSTRACT

We report the discovery of three transiting low-mass companions to aged stars: a brown dwarf (TOI-2336b) and two objects near the hydrogen burning mass limit (TOI-1608b and TOI-2521b). These three systems were first identified using data from the *Transiting Exoplanet Survey Satellite* (*TESS*). TOI-2336b has a radius of $1.05 \pm 0.04\,R_J$, a mass of $69.9 \pm 2.3\,M_J$ and an orbital period of 7.71 d. TOI-1608b has a radius of $1.21 \pm 0.06\,R_J$, a mass of $90.7 \pm 3.7\,M_J$ and an orbital period of 2.47 d. TOI-2521b has a radius of $1.01 \pm 0.04\,R_J$, a mass of $77.5 \pm 3.3\,M_J$, and an orbital period of 5.56 d. We found all these low-mass companions are inflated. We fitted a relation between radius, mass, and incident flux using the sample of known transiting brown dwarfs and low-mass M dwarfs. We found a positive correlation between the flux and the radius for brown dwarfs and for low-mass stars that is weaker than the correlation observed for giant planets. We also found that TOI-1608 and TOI-2521 are very likely to be spin-orbit synchronized, leading to the unusually rapid rotation of the primary stars considering their evolutionary stages. Our estimates indicate that both systems have much shorter spin-orbit synchronization time-scales compared to their ages. These systems provide valuable insights into the evolution of stellar systems with brown dwarf and low-mass stellar companions influenced by tidal effects.

Key words: techniques: photometric – techniques: radial velocities – (stars:) brown dwarfs – stars: low mass.

1 INTRODUCTION

Brown dwarfs are objects with masses between those of giant planets and stars. Typically, the lower mass limit is taken to be $\sim 13\,M_J$ (Burrows et al. 1997; Spiegel, Burrows & Milsom 2011), the minimum mass to ignite deuterium fusion, and the upper mass limit is taken to be $\sim 80\,M_J$ (Baraffe et al. 2002), the minimum mass to ignite ordinary hydrogen fusion. The term 'brown dwarf' was first used by Tarter (1975). Since the earliest brown dwarf discoveries such as Gliese 229B (Nakajima et al. 1995; Oppenheimer et al. 1995) and Teide 1 (Rebolo, Zapatero Osorio & Martín 1995; Rebolo et al. 1996), thousands of isolated brown dwarfs have been discovered (e.g. Henry et al. 2018). However, previous works using radial velocity data have shown that, on relatively short orbital periods, brown dwarf companions around solar-type stars are significantly rarer compared to planetary and stellar companions, which is known

as the 'brown dwarf desert' (e.g. Marcy & Butler 2000; Grether & Lineweaver 2006). Similarly, the known transiting brown dwarfs are outnumbered by hot Jupiters (e.g. the NASA Exoplanet Archive). Despite the similar radii of hot Jupiters and brown dwarfs (Chen & Kipping 2017), only about 30 transiting brown dwarfs have been found, in contrast with the hundreds of transiting hot Jupiters. This desert may result from two different formation mechanisms, i.e. gravitational instability and cloud fragmentation, dominating different mass regimes for the formation of brown dwarfs (see discussion in Palle et al. 2021). For example, Ma & Ge (2014) analysed a catalog of 62 brown dwarf companions and found that they are most depleted at $30\,M_J < M\sin i < 55\,M_J$ and $P < 100$ d. Using $42.5\,M_J$ as a threshold, they found that the eccentricity distribution of lower mass brown dwarfs is consistent with that of massive planets, while the eccentricity distribution of higher mass brown dwarfs is more consistent with that of stellar binaries. They suggested that the brown dwarfs below $42.5\,M_J$ may form through disc gravitational instability, while the brown dwarfs above $42.5\,M_J$ may form through molecular cloud fragmentation like stars. However, the scope and robustness of such statistical works is limited by the small size of

[*] E-mail: lzt22@mails.tsinghua.edu.cn (ZL); tianjungan@gmail.com (TG); sharonw@mail.tsinghua.edu.cn (SXW)

the brown dwarf sample. Therefore, we need more brown dwarf companions with precisely determined parameters such as mass, radius, and age to analyse the origin of the 'brown dwarf desert' and their formation mechanism.

NASA's *Transiting Exoplanet Survey Satellite* (*TESS*) mission (Ricker et al. 2015) is an all-sky transit survey, searching for planets around nearby bright stars, which also provides an exciting opportunity to enlarge the sample of transiting brown dwarfs. *TESS* has completed its primary mission (2018 July–2020 July), where it observed most of the sky, and its First Extended Mission (2020 July–2022 September) where it observed most of the sky a second time, and it is now in its second extended mission (started September 2022) where it continues to re-observe the sky. Up to late 2022, *TESS* has successfully found more than 10 transiting brown dwarfs (e.g. Grieves et al. 2021; Carmichael et al. 2022; Psaridi et al. 2022). Light curves from *TESS* can provide us with the radius of a transiting brown dwarf, its period, and its orbital inclination. However, transit data alone are not sufficient to determine the masses, which are important to distinguish brown dwarfs from planetary-mass companions having similar radii. In addition, mass is a fundamental parameter for brown dwarf population studies as in the works mentioned above. Therefore, we need to observe the spectra of the host stars of transiting brown dwarfs to extract their radial velocities (RVs) and derive the true mass (instead of the minimum mass $m \sin i$) and other orbital parameters such as the eccentricity.

Furthermore, the stellar spectra are crucial for stellar characterization, which will also encompass photometry, parallax, and other potential data. Proper characterization of the host star is important in order to characterize its companions. For instance, to estimate the radius of a companion using transit, the radius of its host star is necessary. Ultimately, a wealth of physical information can be obtained for a transiting brown dwarf system, including the mass, radius, and orbit of the companion. Such systems are essentially ideal samples for further studies such as population statistics and investigations into their formation and evolution scenarios. In addition, only a limited number of field BDs have dynamic mass measurements, and their radii are too small for any 'resolved' measurement even with interferometry. Therefore, transiting brown dwarf systems are the only ideal means to constrain the masses and radii of brown dwarfs, which is essential for the study of these objects.

As different evolution models are developed for brown dwarfs and low-mass stars (e.g. Baraffe et al. 2003; Phillips et al. 2020; Marley et al. 2021), the transiting brown dwarf sample can be used to test these models (e.g. Carmichael et al. 2021). Compared with field brown dwarfs, the transiting ones tend to be better characterized in terms of radius, mass, age and even elemental abundances, thanks to the wealth of information provided by their host stars, for example, assuming they were formed together and co-evolved.

A special stage in the evolution of brown dwarfs in binary systems is when their host stars evolve off the main sequence. Low-mass objects orbiting evolved stars are poorly understood due to the challenges in their detection and characterization largely caused by the large radii and stellar RV jitter of the host stars (Yu et al. 2018; Tayar, Stassun & Corsaro 2019). It has been suggested that planets around evolved stars should be different from planets around main-sequence stars in many aspects due to their dynamical interactions with the evolved host (Veras 2016). For example, the increasing tidal interaction may speed up the orbital decay and planet engulfment (Hut 1981; Jackson, Greenberg & Barnes 2008), which may induce a different eccentricity distribution in the observed population of surviving hot Jupiters (Villaver et al. 2014; Grunblatt et al. 2018). Additionally, due to the increasing luminosity of the evolved host

stars, close-in planets would receive more flux, which makes such systems ideal for studies of planet inflation (e.g. Grunblatt et al. 2022; Saunders et al. 2022) or re-inflation (e.g. Grunblatt et al. 2016). In contrast to the numerous works on planets around evolved stars, few works discuss brown dwarfs or very low-mass stars around evolved stars, probably due to the small sample size of such systems. Do low-mass stars and brown dwarfs around evolved stars undergo orbital or radius changes in a similar way as planets? Gathering a sample of well-characterized transiting brown dwarfs would be the crucial first step in addressing this question.

The tidal effect plays a crucial role in the evolution of binary systems. For instance, it has been observed that the rotation of close binary stars tends to synchronize with their orbital motion due to tidal interactions (e.g. Levato 1974; Giuricin, Mardirossian & Mezzetti 1984). However, for planetary systems, the rotations of the host stars are rarely synchronized with the orbits (though suspected, e.g. in Donati et al. 2008). This is primarily because the angular momentum of planetary orbits is often insufficient to significantly influence the rotation of the host stars. Therefore, brown dwarf companions, which serve as transitional objects between planets and stars, can offer ideal examples to study tidal effects under different companion masses. Furthermore, brown dwarf companions can also provide valuable insights into the theories about the conditions for tidal synchronization and tidal equilibrium (e.g. Hut 1980).

Here, we report the discovery of a transiting brown dwarf, TOI-2336b, and two transiting objects near the hydrogen burning mass limit, TOI-1608b and TOI-2521b, around three aged stars using *TESS* data and ground-based follow-up observations.[1] In Section 2, we describe the data we used in this work. Section 3 presents the analyses to determine the properties of the host stars of these three systems. Section 4 presents the joint analysis of the light curves and the RV data and how we obtained the orbital parameters of the companions. In Section 5, we analyse the radius inflation of brown dwarfs and low-mass stars, and we discuss the tidal evolution of these systems. We conclude our findings in Section 6.

2 OBSERVATIONS

2.1 *TESS* photometry

TOI-1608 (TIC 138017750) was observed with the 2-min cadence exposures in *TESS* Sector 18 from 2019 November 3 to 2019 November 27. The photometry were extracted by the science processing operation centre (SPOC; Jenkins et al. 2016) pipeline. SPOC produces two kinds of light curves, using simple aperture photometry (SAP) or the Presearch Data Conditioning SAP (PDCSAP; Smith et al. 2012; Stumpe et al. 2012, 2014). PDCSAP is corrected for the instrumental systematic effects and dilution, and we used PDCSAP light curves in our analysis. Eight transit signals were identified in this light curve with a period of 2.47 d. SPOC DV reports (Twicken et al. 2018; Li et al. 2019) present the difference image centroiding results of TOI-1608, which indicates that the source of the transit signal is located within 1.3 ± 2.5 arcsec of the target star, complementing the results of the high-resolution imaging presented in Section 2.4.

TOI-2336 (TIC 88902249) was observed with the 30-min cadence exposures in *TESS* Sector 11 from 2019 April 23 to May 20, and it was re-observed with the 10-min cadence exposures in *TESS*

---

[1]These three old stars have slightly evolved off the main sequence and are not all into the subgiant phase yet, so we refer to them as 'aged' instead of evolved stars to be precise.
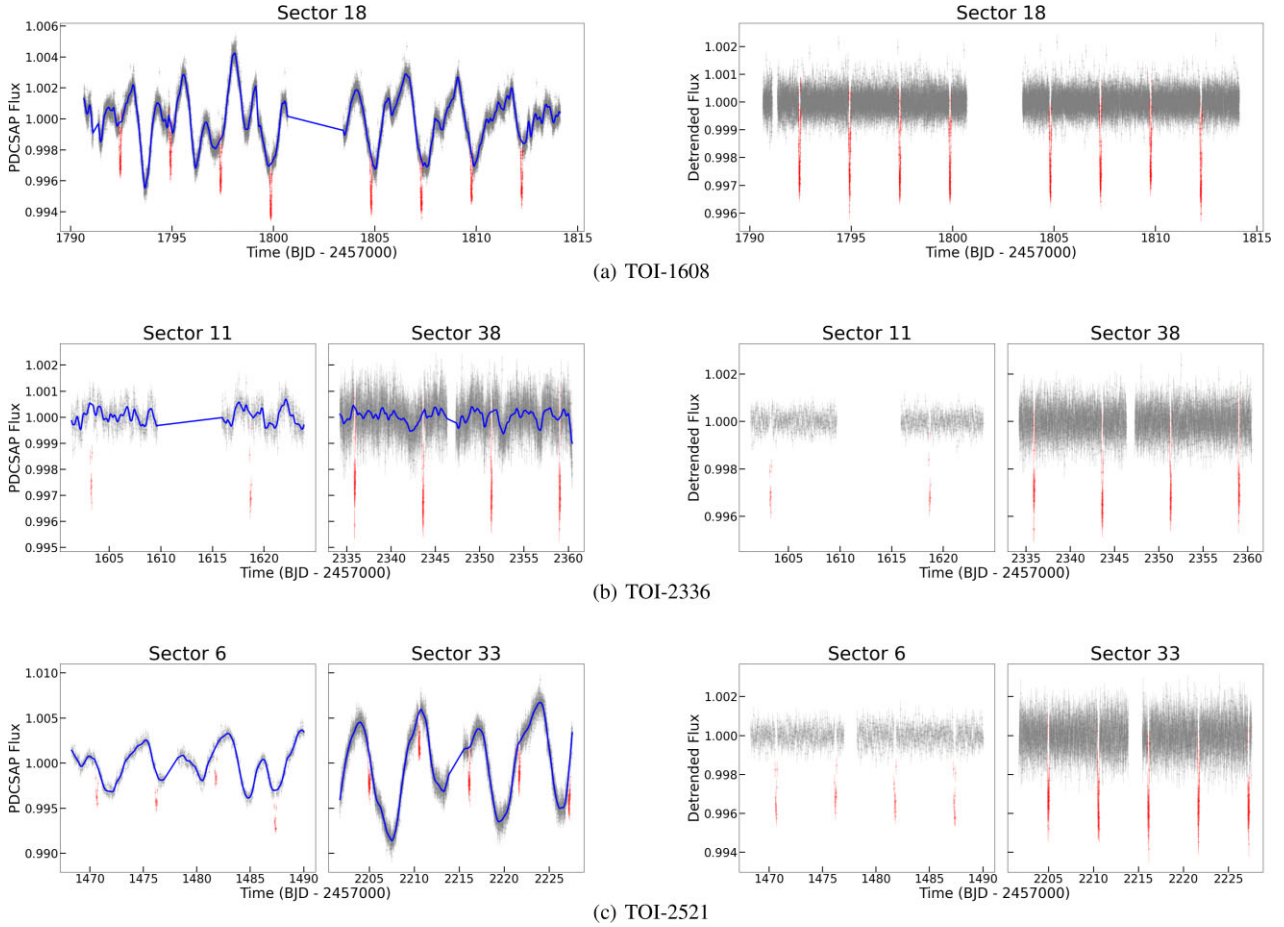
Figure 1. *TESS* light curves of TOI-1608, TOI-2336, and TOI-2521. Left-hand panels: The dots are the *TESS* PDCSAP data and the red dots highlight the transit signals. The blue lines are the best-fitting GP models for detrending. The sector 18 for TOI-1608 was observed with the 2-min cadence exposures. The sector 11 for TOI-2336 and the sector 6 for TOI-2521 were observed with the 30-min cadence exposures. The sector 38 for TOI-2336 and the sector 33 for TOI-2521 were observed with the 10-min cadence exposures. Right-hand panels: The final detrended *TESS* PDCSAP light curves.

Sector 38 from 2021 April 29 to May 26 during the *TESS* First Extended Mission. Both light curves were extracted by the TESS-SPOC pipeline (Caldwell et al. 2020) and we used the PDCSAP in our analysis. Two transit signals were identified in the 30-min data and four transit signals were identified in the 10-min data with a period of 7.71 d. The TESS-SPOC DV reports of Sector 38 presents the difference image centroiding results of TOI-2336, which indicates that the source of the transit signal is located within 3.8 ± 2.5 arcsec of the target star, complementing the results of the high-resolution imaging presented in Section 2.4.

TOI-2521 (TIC 72556406) was observed with the 30-min cadence exposures in *TESS* Sector 6 from 2018 December 15 to 2019 January 6, and it was re-observed with the 10-min cadence exposures in *TESS* Sector 33 from 2020 December 18 to 2021 January 13 during the *TESS* First Extended Mission. Again we used the PDCSAP light curves extracted by the TESS-SPOC pipeline (Caldwell et al. 2020) in our analysis. Four transit signals were identified in the 30-min data and five transit signals were identified in the 10-min data with a period of 5.56 d.

We obtained all *TESS* data from the Mikulski Archive for Space Telescopes (MAST) Portal[2]. We then detrended the *TESS* light curve

to remove the remaining systematic trends by fitting a Gaussian Process (GP) model after masking out the in-transit data using the JULIET package (Espinoza, Kossakowski & Brahm 2019), which employs the package CELERITE (Foreman-Mackey et al. 2017) to build the GP model. The PDCSAP light curves with the best-fitting GP models are shown in Fig. 1.

2.2 Ground-based photometry

2.2.1 LCOGT

We conducted ground-based follow-up observations of TOI-2336 using the Las Cumbres Observatory Global Telescope (LCOGT[3]) network (Brown et al. 2013) on 2021 July 1. We used the TESS TRANSIT FINDER, which is a customized version of the TAPIR software package (Jensen 2013), to schedule the transit observation. The observation was taken using the 1.0-m telescopes located at Cerro Tololo Interamerican Observatory (CTIO). The images were acquired with the Sinistro cameras in the Pan-STARRS z-short band (z_s) with an exposure time of 30 s. The photometric analysis was then carried out using ASTROIMAGEJ (Collins et al. 2017).

[2]https://mast.stsci.edu/portal/Mashup/Clients/Mast/Portal.html

[3]https://lco.global/
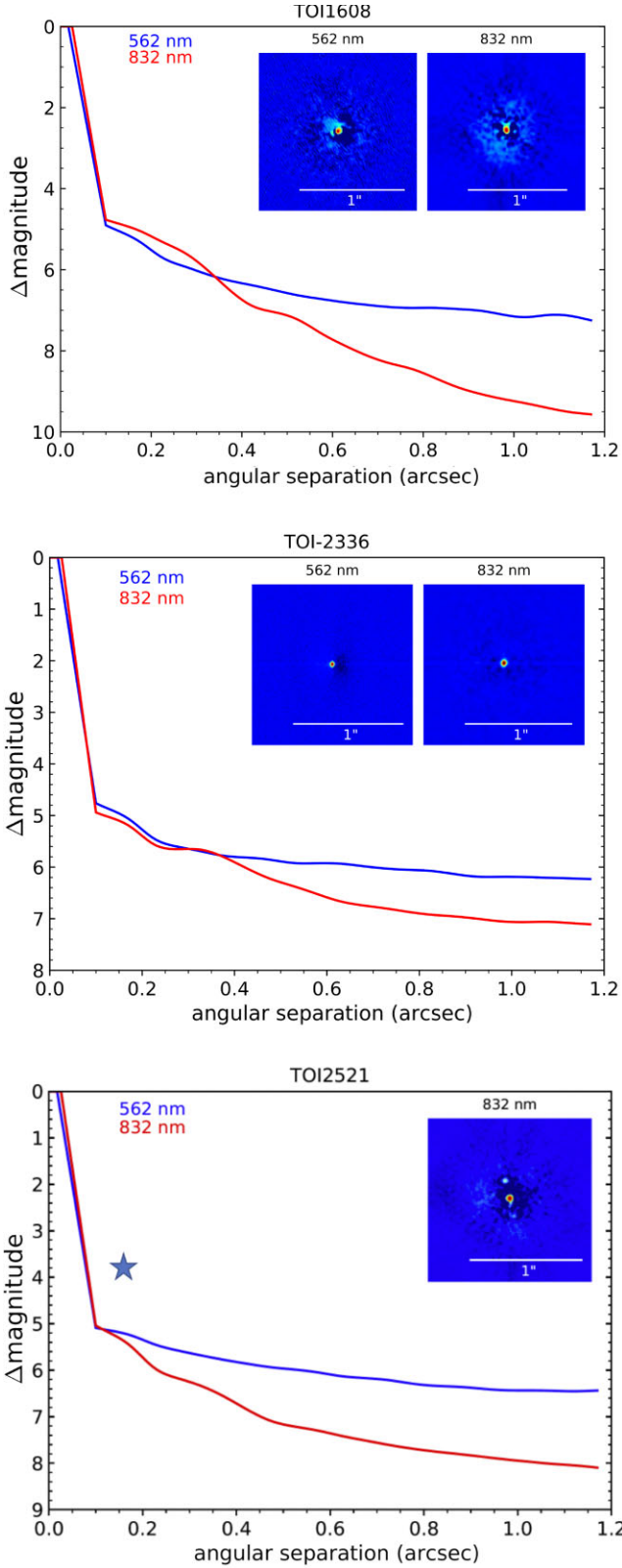
Figure 2. We show the 5σ speckle imaging contrast curves in both filters as a function of the angular separation from the diffraction limit out to 1.2 arcsec. The inset shows the reconstructed 832 nm image with a 1 arcsec scale bar. For TOI-1608 and TOI-2336, our results rule out companions and background objects that are potentially problematic. For TOI-2521, the blue star symbol shows its faint close companion. With a magnitude of 3.94 fainter, the companion will not influence our analysis.
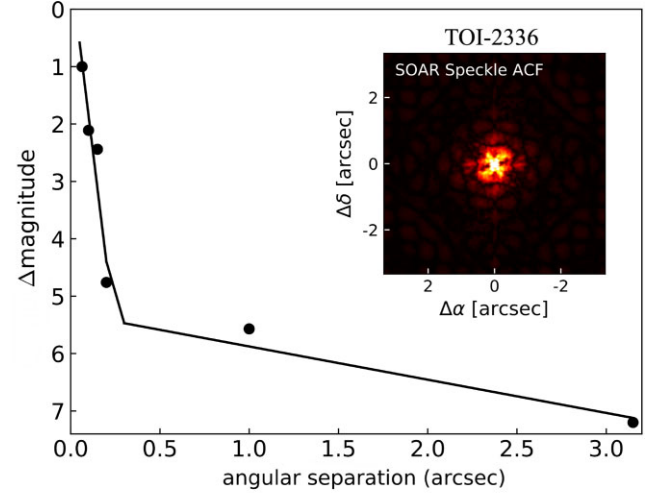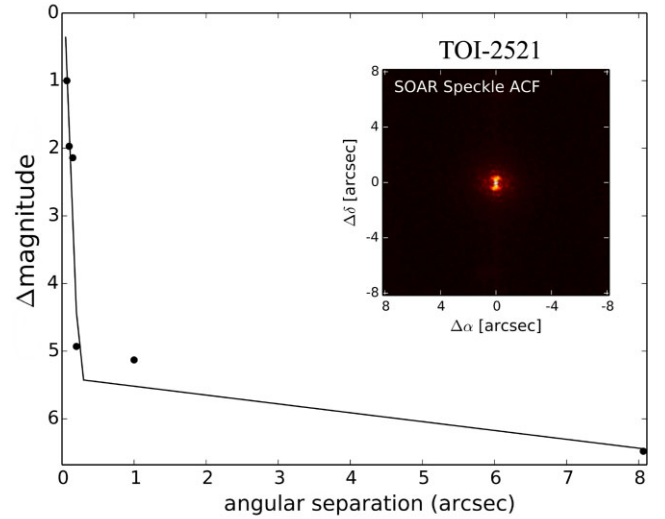

Figure 3. Speckle autocorrelation functions for TOI-2336 and TOI-2521 obtained in the *I* band using SOAR. The 5σ contrast curves are shown as the black points. The black solid line shows the linear fit of the data.

2.2.2 WASP

WASP-South has an array of 8 cameras forming the South African station of the WASP transit-search survey (Pollacco et al. 2006). The field of TOI-2336 was observed during 2006, 2007, and 2008, and then again in 2011 and 2012. Within each year, observations of the field every ∼ 15 min were obtained on each clear night, over a span of ∼ 150 nights. During that time, WASP-South was equipped with 200 mm, f/1.8 lenses, observing with a 400–700 nm bandpass, and with a photometric extraction aperture of 48 arcsecs. A total of 32 000 photometric data points were obtained.

TOI-2336 was not selected as a WASP candidate, but with hindsight we find that the standard WASP search algorithm (Collier Cameron et al. 2007) produces a match to the *TESS* transit detection with a period of 7.712 d.

We also searched the WASP data for signs of a stellar rotational modulation, using the methods from Maxted et al. (2011), but found only a 95 per cent upper limit of 1 mmag on any modulation in the range of 1–100 d.
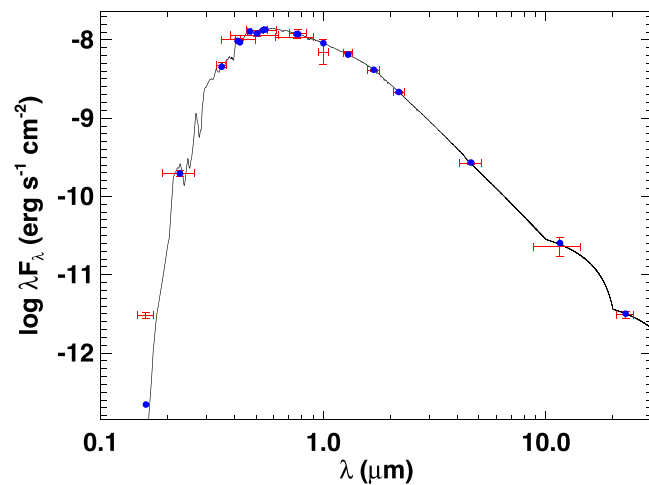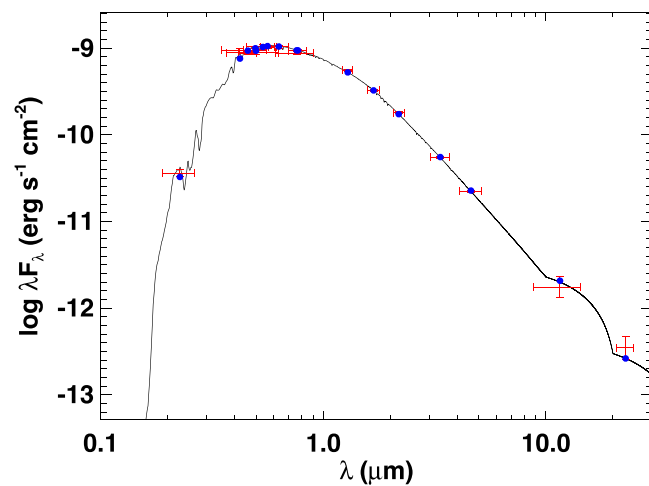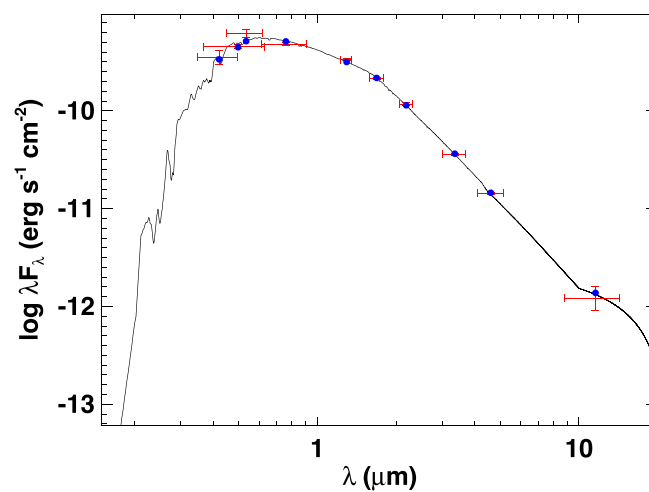
Figure 4. SED of TOI-1608 (top), TOI-2336 (middle), and TOI-2521 (bottom). Red symbols represent the observed photometric measurements, where the horizontal bars represent the effective width of the passband. Blue symbols are the model fluxes from the best-fitting Kurucz atmosphere model (black).
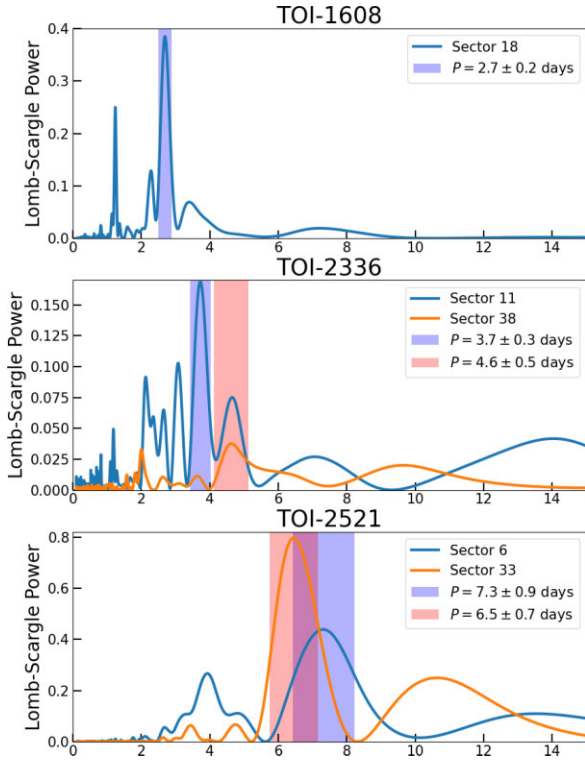
Figure 5. The generalized Lomb–Scargle periodogram from the *TESS* PDCSAP light curves of TOI-1608, TOI-2336, and TOI-2521. The periods of the highest peaks in each periodogram are marked as different colour bars.

2.3 Spectroscopic observations

2.3.1 NRES

We acquired 16 spectra for TOI-1608 from 2021 December 3 to 2022 January 9 at the McDonald Observatory, and 21 spectra for TOI-2336 between 2021 April 22 and 2021 July 19 at South African Astronomical Observatory (SAAO) using the LCOGT Network of Robotic Echelle Spectrographs (NRES; Siverd et al. 2018). NRES has four sets of identical echelle spectograph units at four LCOGT sites. It has a resolving power of $R \sim 53\,000$, covering a wavelength range from 3900 to 8600 Å. We reduced the spectra and extracted the RVs using the CERES pipeline (Brahm, Jordán & Espinoza 2017).

2.3.2 CHIRON

We observed TOI-2336 and TOI-2521 with the CHIRON fibre-fed echelle spectrograph at the SMARTS 1.5-m telescope located at Cerro Tololo Inter-American Observatory, Chile (Tokovinin et al. 2013). CHIRON is a high-resolution echelle spectrograph with a spectral coverage of 4100 to 8700 Å. Both targets were observed in the *fiber* mode, with a spectral resolving power of $R \sim 28\,000$. For TOI-2336, we obtained 12 spectra from 2021 May 7 to August 5 with an exposure time of 1200 s. For TOI-2521, we gathered 8 RVs, from 2021 March 20 to March 30, using an exposure time of 1800 s. We used the spectra extracted via the official CHIRON pipeline as per Paredes et al. (2021). Radial velocities were derived from a least-squares deconvolution between the observation and a non-rotating synthetic template, generated using the ATLAS9 atmosphere models (Castelli & Hubrig 2004) at the spectral parameters of the targets. The derived broadening profile is fitted with a kernel accounting for the effects of rotational, macroturbulent, instrumental broadening,
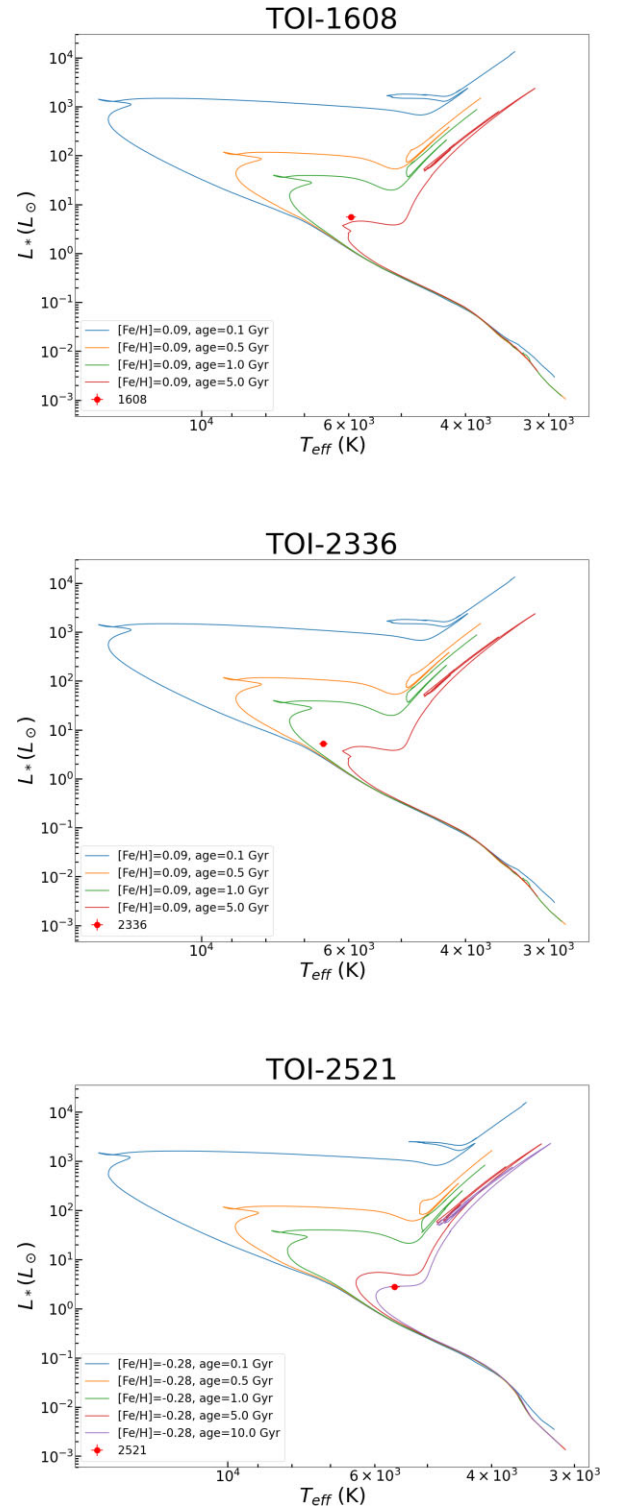
Figure 6. TOI-1608, TOI-2336, and TOI-2521 in HR diagrams. We also plot several isochrones of different ages as a comparison. These diagrams show that all of our targets have evolved a little off the main sequence and are consistent with being old stars.
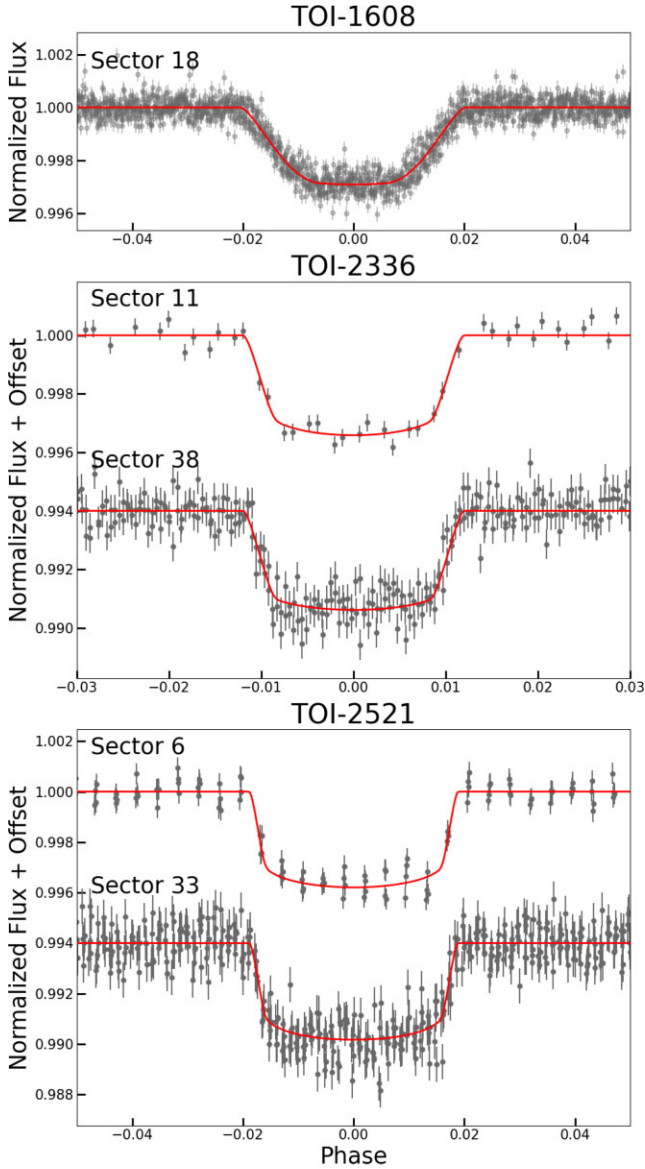
Figure 7. The *TESS* light curves near the transit of TOI-1608, TOI-2336, and TOI-2521 with arbitrary offsets. The red line is the best-fitting transit model obtained by JULIET. The grey dots are the *TESS* data.

and radial velocity shift. Spectroscopic atmosphere parameters were derived by matching the observed CHIRON spectra against a library of 10 000 observed spectra previously classified via the Stellar Parameter Classification (Buchhave et al. 2012). The library is convolved to the instrument resolution of CHIRON and interpolated via a gradient-boosting regressor. Uncertainties on the spectroscopic parameters are determined by the spectrum-to-spectrum scatter of these values.

2.3.3 *CORALIE*

We used the high-resolutionWe used the high-resolution spectrograph CORALIE to obtain spectra for TOI-2336. CORALIE is installed at the Swiss 1.2-m Leonhard Euler Telescope at La Silla Observatory, Chile (Queloz et al. 2001), and it has a resolution of $R = 60\,000$ and is fed by a 2 fibre. We acquired 16 RV measurements from 2021 April 14 to June 08 with exposure times ranging between
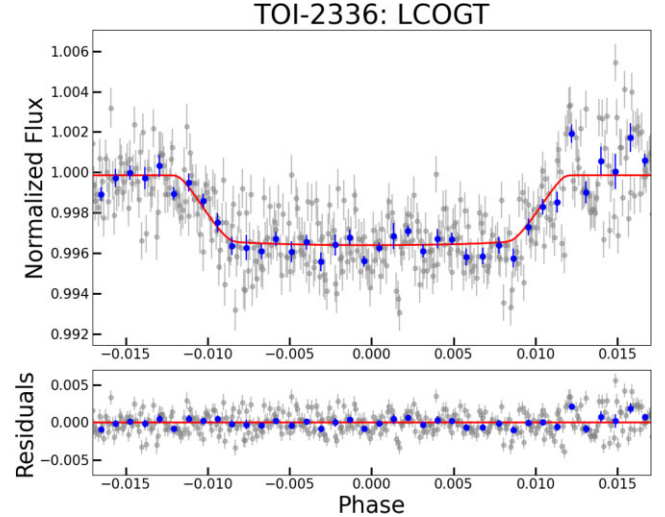
Figure 8. The *LCOGT* light curves of TOI-2336 in the Pan-STARRS z-short ban (z_S). The red line is the best-fitting transit model obtained by JULIET. The grey dots are the *LCOGT* data and the blue dots are binned data.

1200 s and 2400 s and S/N between 15 and 33. The RV measurement of each epoch was extracted by cross-correlating the spectrum with a binary G2 mask (Pepe et al. 2002). The bisector-span (BIS), the contrast (depth), and the full width at half-maximum (FWHM) were recorded using the standard CORALIE data reduction pipeline.

2.3.4 *TRES*

We observed TOI-1608 and TOI-2521 with the Tillinghast Reflector Echelle Spectrograph (TRES; Fűrész 2008). TRES is a fibre-fed echelle spectrograph mounted on the 1.5 m telescope at the Fred Lawrence Whipple Observatory (FLWO) in Arizona. TRES covers a wavelength range of 3900–9100 Å and has a resolving power of $R \sim 44\,000$. Two reconnaissance spectra of TOI-1608 were obtained on 2019 December 31 and 2020 January 4 and similarly two reconnaissance spectra of TOI-2521 were obtained on 2021 March 11 and March 19. The spectra were extracted as described in Buchhave et al. (2010) and were then used to derive stellar parameters using the Stellar Parameter Classification (SPC; Buchhave et al. 2012) tool. SPC cross-correlates the observed spectrum against a grid of synthetic spectra derived from the Kurucz atmospheric models (Kurucz 1992). SPC was used to derive parameters $T_{\rm eff}$, [m/H], and $v\sin i_*$ by fixing the $\log g_*$ from isochrone fitting as described in Section 3.2. We did not use the TRES spectra for RV measurements, as they include only two epochs for each of TOI-1608 and TOI-2521.

2.4 High angular resolution imaging

The presence of a close companion star can be the cause of a transit-like event (i.e. a false positive) can cause incorrect stellar and exoplanet parameters to be determined (Furlan & Howell 2017, 2020), or can lead to non-detections of small planets residing with the same exoplanetary system (Lester et al. 2021). Given that nearly one-half of FGK stars are in binary or multiple star systems (Matson, Howell & Ciardi 2019), high-resolution imaging provides crucial information toward our understanding of exoplanetary formation, dynamics and evolution (Howell et al. 2021). We conducted high-resolution imaging observations on the three systems and summarize our imaging observations and results in this section.

2.4.1 Gemini

TOI-1608 was observed on 2022 February 10 UT using the 'Alopeke speckle instrument on the Gemini North 8-m telescope, TOI-2336 was observed on 2022 May 05 UT using the Zorro instrument on the Gemini South 8-m telescope (Scott et al. 2021; Howell & Furlan 2022). TOI-2521 was observed on 2023 January 8 UT using the Zorro speckle instrument on the Gemini South 8-m telescope.

'Alopeke and Zorro both provide simultaneous speckle imaging in two bands (562 and 832 nm) with output data products including a reconstructed image with robust contrast limits on companion detections (e.g. Howell et al. 2016).

For TOI-1608 and TOI-2336, three sets of 1000×0.06 s images were obtained and processed in our standard reduction pipeline (Howell et al. 2011). Fig. 2 shows our final contrast curves and the 832 nm reconstructed speckle image. We find that both TOI-1608 and TOI-2336 have no stellar companions brighter than 5–9 mag below that of the target star from the 8-m telescope diffraction limit (20 mas) out to 1.2 arcsec. At the distance of TOI-1608 (d =101 pc), these angular limits correspond to (sky-projected) spatial limits of 2–120 au and for TOI-2336 ($d = 297$ pc) the angular limits correspond to 6–358 au. Objects that are 5–9 mag fainter than TOI-1608 (an F5 star) or TOI-2336 (an F4 star) will be late K-dwarfs or smaller objects (Pecaut, Mamajek & Bubar 2012; Pecaut & Mamajek 2013), and will not have any significant impact on our analysis.

For TOI-2521, five sets of 1000×0.06 s images were obtained during a time of good seeing (0.47 arcsec) and processed in our standard reduction pipeline. Fig. 2 shows our achieved 5σ magnitude contrast curves and the 832 nm reconstructed image. The resulting high-resolution imaging revealed that TOI-2521 has a very close companion star. The companion, only detected in the 832 nm band, lies 0.162 arcsec away at a position angle of 16.44 degrees. The close companion is 3.94 magnitudes fainter than the (G8) primary star, suggesting that it is near spectral type M6, in agreement with its red-only detection. Ciardi et al. (2015) showed that 'third-light' contamination from a close companion will cause the determined exoplanet radius to be underestimated, however, at a magnitude difference of 3.94, the contamination due to the faint companion would cause a <1 per cent error in the transit derived exoplanet size. At a separation of 0.162 arcsec, it is 99 per cent probable that the companion is bound (Matson et al. 2018). Our SOAR observation did not detect this companion, which is consistent with the precision of the instrument. No additional close companions were detected near TOI-2521 to within the contrast limits of 5–8 mag over the angular limits of the diffraction limit out to 1.2 arcsec. At the distance of TOI-2521 ($d = 334$ pc), these angular limits correspond to spatial limits of 6.8–409 au.

2.4.2 SOAR

We searched for stellar companions to TOI-2336 and TOI-2521 with speckle imaging on the 4.1-m Southern Astrophysical Research (SOAR) telescope (Tokovinin 2018) on 2021 February 7 UT and 2021 October 1, respectively. The observations were performed in Cousins *I* band, a similar visible bandpass as *TESS*. Both observations were sensitive to an approximately 5-mag fainter star at an angular distance of 0.25 arcsec from the target. More details of the observations within the SOAR *TESS* survey are available in Ziegler et al. (2020). The 5σ detection sensitivity and speckle autocorrelation functions from the observations are shown in Fig. 3. No nearby stars were detected within 3 arcsec of either TOI-2336 or TOI-2521 in the SOAR observations.

3 STELLAR PROPERTIES

In this section, we present the characterization of the host stars of the three targets. Briefly, we first performed an analysis of the broadband spectral energy distribution (SED) in Section 3.1. Then in Section 3.2 we perform isochrone fitting utilizing the T_{eff}, [Fe/H] and log g from SED fitting, the photometry of various bands, and the density derived from the transit model. Additionally, we performed independent spectral analyses in Section 3.3 to validate the results from the isochrone fitting. Finally, we adopted the results from the isochrone fitting as the stellar parameters. Sections 3.4–3.6 are further discussion regarding the stellar rotation, age, and asteroseismology, respectively. All of the adopted stellar parameters are listed in Table 1.

3.1 Spectral energy distribution

As an independent determination of the basic stellar parameters, we performed an analysis of the broadband SED of each star together with the *Gaia* EDR3 parallax (with no systematic offset applied; see e.g. Stassun & Torres 2021), in order to determine an empirical measurement of the stellar radius, following the procedures described in Stassun & Torres (2016), Stassun, Collins & Gaudi (2017), and Stassun et al. (2018a). Depending on the photometry available for each source, we pulled the $B_T V_T$ magnitudes from *Tycho-2*, the *BVgri* magnitudes from *APASS*, the Strömgren *uvby* magnitudes from Paunzen (2015), the JHK_S magnitudes from *2MASS*, the W1–W4 magnitudes from *WISE*, the $GG_{BP}G_{RP}$ magnitudes from *Gaia*, and the FUV and/or NUV fluxes from *GALEX*. All these magnitudes are shown in Table 1. Together, the available photometry spans the stellar SED over the approximate wavelength range 0.2–22 μm (see Fig. 4).

We performed fits to the photometry using Kurucz stellar atmosphere models, with the free parameters being the effective temperature (T_{eff}), metallicity ([Fe/H]), and surface gravity (log g_*). We also fit for the extinction, A_V, limited to the full line-of-sight value from the Galactic dust maps of Schlegel, Finkbeiner & Davis (1998). The resulting fits shown in Fig. 4 have a reduced χ^2 ranging from 1.2 to 1.5, and the best-fitting parameters are summarized in Table 2.

Integrating the model SED gives the bolometric flux at Earth, F_{bol}. Taking the F_{bol} together with the *Gaia* parallax directly gives the luminosity, L_{bol}. Similarly, the F_{bol} together with the T_{eff} and the parallax gives the stellar radius, R_*. Moreover, the stellar mass, M_*, can be estimated from the empirical eclipsing-binary based relations of Torres, Andersen & Giménez (2010). When available, the *GALEX* photometry allows the activity index, log R'_{HK} to be estimated from the empirical relations of Findeisen, Hillenbrand & Soderblom (2011). All quantities are summarized in Table 2.

3.2 Isochrone fitting

In order to obtain more precise stellar parameters, we performed isochrone fitting with the package ISOCHRONES (Morton 2015) based on the results of the SED fitting and the photometry. We pulled T_{eff}, [Fe/H] and log g from SED fitting, the *TESS* magnitudes from TICv8, the JHK_S magnitudes from *2MASS*, the W1–W3 magnitudes from *WISE* and the $GG_{BP}G_{RP}$ magnitudes from *Gaia* DR3. We also used the *Gaia* DR3 parallax as well as the stellar density from the transit model, which is described in Section 4.

Table 1. Adopted stellar parameters for TOI-1608, TOI-2336, and TOI-2521.

Parameter	TOI-1608	TOI-2336	TOI-2521	Source
Main identifiers				
TIC	138017750	88902249	72556406	
Gaia ID	125548289270234880	6206457922905803392	3005862518856922752	
Equatorial Coordinates				
RA	3:23:12.28	15:20:55.30	6:14:06.99	*Gaia* DR3[1]
Dec.	33:04:41.25	−33:41:32.87	−8:03:44.31	*Gaia* DR3
Photometric properties				
TESS (mag)	7.42812 ± 0.0064	10.1757 ± 0.0061	10.8218 ± 0.0065	TICv8[2]
Gaia (mag)	7.8280 ± 0.0004	10.5905 ± 0.0002	11.2692 ± 0.0008	*Gaia* DR3
Gaia BP (mag)	8.1097 ± 0.0016	10.8992 ± 0.0006	11.6116 ± 0.0024	*Gaia* DR3
Gaia RP (mag)	7.3789 ± 0.0012	10.1146 ± 0.0004	10.7518 ± 0.0018	*Gaia* DR3
B (mag)	8.519 ± 0.027	11.134 ± 0.119	12.076 ± 0.231	Hipparcos
V (mag)	7.96 ± 0.03	10.756 ± 0.009	11.263 ± 0.017	Hipparcos
J (mag)	6.885 ± 0.027	9.61 ± 0.024	10.161 ± 0.026	2MASS[3]
H (mag)	6.636 ± 0.017	9.386 ± 0.026	9.839 ± 0.023	2MASS
K (mag)	6.584 ± 0.029	9.283 ± 0.019	9.743 ± 0.019	2MASS
*WISE*1 (mag)	7.571 ± 0.402	9.247 ± 0.023	9.707 ± 0.023	*WISE*[4]
*WISE*2 (mag)	6.554 ± 0.024	9.247 ± 0.02	9.726 ± 0.021	*WISE*
*WISE*3 (mag)	6.604 ± 0.015	9.195 ± 0.039	9.688 ± 0.043	*WISE*
*WISE*4 (mag)	6.52 ± 0.072	8.49 ± 0.331	9.193[a]	*WISE*
Astrometric properties				
ϖ (mas)	9.87 ± 0.04	3.37 ± 0.02	2.99 ± 0.02	*Gaia* DR3
μ_α (mas yr^{-1})	109.30 ± 0.04	6.22 ± 0.02	−7.68 ± 0.03	*Gaia* DR3
μ_δ (mas yr^{-1})	−58.30 ± 0.03	−18.97 ± 0.02	−0.37 ± 0.03	*Gaia* DR3
RV (km s^{-1})	44.5 ± 2.8	35.6 ± 1.5	−32.5 ± 2.0	*Gaia* DR3
Derived parameters				
Distance (pc)	101.3 ± 0.4	296.6 ± 1.7	334.4 ± 2.3	Section 3.2
M_* (M$_\odot$)	1.31 ± 0.07	1.40 ± 0.07	0.95 ± 0.06	Section 3.2
R_* (R$_\odot$)	2.16 ± 0.08	1.82 ± 0.06	1.74 ± 0.06	Section 3.2
ρ_* (g cm^{-3})	0.18 ± 0.03	0.33 ± 0.04	0.25 ± 0.03	Section 3.2
log g_*	3.89 ± 0.04	4.06 ± 0.04	3.93 ± 0.04	Section 3.2
L_* (L$_\odot$)	5.56 ± 0.26	5.10 ± 0.21	2.74 ± 0.12	Section 3.2
$T_{\rm eff}$ (K)	6028 ± 82	6433 ± 84	5625 ± 74	Section 3.2
[Fe/H] (dex)	0.09 ± 0.12	0.09 ± 0.11	−0.28 ± 0.13	Section 3.2
Age (Gyr)	4.0 ± 0.8	2.4 ± 0.5	10.1 ± 1.1	Section 3.2
$P_{\rm rot}$ (d)	2.7 ± 0.2	4.2 ± 0.5	6.9 ± 0.9	Section 3.4

[a]The *WISE* catalog did not report an uncertainty for this *W*4 magnitude for TOI-2521. Therefore, we did not use this magnitude in our analysis.
References: [1] Gaia Collaboration (2021), [2] Stassun et al. (2018b, 2019), [3] Cutri et al. (2003), [4] Wright et al. (2010).

Table 2. Summary of derived and empirical parameters determined from fits to the stellar spectral energy distributions in Section 3.1. $T_{\rm eff}$, [Fe/H], and log g_* here are used as the input of isochrone fitting in Section 3.2.

Parameter	TOI-1608	TOI-2336	TOI-2521
A_V	0.01 ± 0.01	0.44 ± 0.03	0.07 ± 0.07
$T_{\rm eff}$ (K)	5950 ± 100	6550 ± 100	5600 ± 100
[Fe/H]	0.1 ± 0.3	0.0 ± 0.3	−0.3 ± 0.3
log g_*	4.0 ± 0.5	4.2 ± 0.3	4.0 ± 0.3
$F_{\rm bol}$ (10^{-9} erg s^{-1} cm^{-2})	17.40 ± 0.20	1.918 ± 0.045	0.793 ± 0.018
$L_{\rm bol}$ (L$_\odot$)	5.564 ± 0.068	5.25 ± 0.13	2.771 ± 0.068
R_* (R$_\odot$)	2.222 ± 0.076	1.781 ± 0.059	1.770 ± 0.068
M_* (M$_\odot$)	1.38 ± 0.08	1.41 ± 0.08	1.10 ± 0.07
log $R'_{\rm HK}$	− 4.52 ± 0.05	–	–

In the results of TOI-1608, we find bimodality in the posterior distribution of M_*, ρ_*, log g_* and age, which is shown in Fig. A1. We compared the best-fitting values of these two peaks with the SED fitting results and the *Gaia* DR3 Final Luminosity Age Mass Estimator (FLAME) results (Gaia Collaboration 2016, 2021), and we found that the results of the posterior peak with a lower mass estimate are more consistent with the SED fitting and *Gaia* DR3. Therefore, we adopted

the set of posterior distributions with a lower mass to derive the final stellar parameters and uncertainties from the isochrone fitting for TOI-1608.

Similarly for TOI-2521, we checked for consistency and find that the mass estimates are different in these three sets of results. The mass values are $1.10 \pm 0.07\,M_*$, $0.95 \pm 0.06\,M_*$, and $1.05 \pm 0.04\,M_*$ from the SED fitting, isochrone fitting and *Gaia* DR3, respectively. Relatively speaking, the mass derived from the SED fitting using the empirical relation from Torres et al. (2010) is not as accurate as the other two estimates because the Torres et al. (2010) relation probably does not work very well for aged stars due to the limit of their stellar sample. We consider the mass from our isochrone fitting as the more reliable one, as we incorporated the results from the SED fitting and also used more photometric data than *Gaia* DR3. Therefore, we adopted the results from our isochrone fitting as the final stellar parameters for TOI-2521.

For TOI-2336, our results from the isochrone fit are consistent with the SED fitting and *Gaia* DR3, so we adopted the isochrone fitting results as the final stellar parameters to stay consistent with the other two targets. The final stellar parameters we adopted in the following analyses are summarized in Table 1.

Table 3. Summary of derived parameters determined from CHIRON and TRES spectra analysis.

Parameter	TOI-1608	TOI-2336	TOI-2521
CHIRON			
$T_{\rm eff}$ (K)	–	6551 ± 100	5526 ± 50
[Fe/H] (dex)	–	-0.03 ± 0.10	-0.41 ± 0.10
$\log g_*$	–	4.16 ± 0.10	3.70 ± 0.10
$v \sin i$ (km s^{-1})	–	29.7 ± 0.5	15.6 ± 0.5
TRES			
$T_{\rm eff}$ (K)	6051 ± 56	–	5604 ± 50
[M/H] (dex)	0.10 ± 0.08	–	-0.21 ± 0.08
$v \sin i$ (km s^{-1})	48.3 ± 0.5	–	15.2 ± 0.5

3.3 Spectral analysis

We analysed CHIRON and TRES spectra to derive the stellar parameters. The observations and analyses are described in Sections 2.3.2 and 2.3.4, and the results are shown in Table 3. $T_{\rm eff}$ from both CHIRON and TRES and [Fe/H] from CHIRON are consistent with the results from other methods. [M/H] from TRES is obtained by using all of the lines in the wavelength region from ~505 to ~536 nm. As iron lines dominate in this range, we compare these results with [Fe/H] from other methods and found they agree with each other. However, $\log g_*$ for TOI-2521 from CHIRON spectra is not consistent with isochrone fitting because TOI-2521 is a fast rotating star, where the spectra would have a relatively poor constraint on $\log g_*$. Thus, we only use the spectroscopic results as a check and adopt the results from isochrone fitting for further analyses.

3.4 Stellar rotation period

We masked in-transit data points in the *TESS* PDCSAP light curves (shown in the left-hand panels of Fig. 1) and used Generalized Lomb–Scargle periodograms to estimate the stellar rotation period of TOI-1608, TOI-2336, and TOI-2521. The Lomb–Scargle periodograms are shown in Fig. 5. We attributed the highest peak in the Lomb–Scargle periodogram to the stellar rotation period. For each peak, we used half of its FWHM as the uncertainty. For TOI-2336 and TOI-2521, we find the results obtained from different sectors are consistent. We used the average of different sectors as the final rotation period and use the higher uncertainty as the final error estimation. The final results are listed in Table 1. Using these rotation period and R_* derived in Section 3.2, we can calculate the rotational velocities of TOI-1608, TOI2336, and TOI-2521 to be 40.5 ± 3.5, 21.9 ± 3.1, and 12.8 ± 1.9 km s^{-1}, respectively. Compared with $v \sin i$ derived from the spectra, the velocities of TOI-1608 and TOI-2336 are about 2σ smaller and the velocity of TOI-2521 is about 1σ smaller, which is unphysical (though still roughly consistent statistically speaking). This may result from the unreliable $v \sin i$ estimates from spectral analyses caused by the fast rotation and low $\log g_*$ of these three targets, or it may result from our estimates of the rotation period using the *TESS* light curves, which have a limited baseline. More accurate measurements on $v \sin i$ and the rotation period in the future would be able to put constraints on the projected stellar obliquity (Masuda & Winn 2020).

3.5 Stellar age

We determined the ages of these three stars from isochrone fitting in Section 3.2 and their rotational periods in Section 3.4. However, their rotations seem to be too fast for their ages. For example, according to Fig. 7 in Curtis et al. (2020), the rotational period of TOI-2521 should be larger than 20 d as its age is larger than 3 Gyr, which is not consistent with its measured rotational period of ~7 d. Therefore, we adopted several methods to check whether these three stars are indeed old stars.

We compared these three targets with stellar evolution models in the Hertzsprung–Russell (HR) diagram (Fig. 6). We used the package ISOCHRONES that adopted MIST model (Dotter 2016) to plot the isochrones in Fig. 6. As a result, we can see that all these three targets have evolved a little off the main sequence and are consistent with the old ages instead of young ages. In addition, we check the lithium absorption lines in the CHIRON and TRES spectra of these targets and found essentially no Li absorption, which also supports the old ages. Therefore, we conclude that all our targets are indeed old stars.

We also found explanations for the fast rotation of these three stars. For TOI-1608 and TOI-2521, we found that tidal spin-orbit synchronization can account for their fast rotation. We discuss this scenario in detail in Section 5.2.2. For TOI-2336, we found that, given its effective temperature of 6433 ± 84 K and mass of $1.40 \pm 0.07\,M_*$, its fast rotation is not conflict with gyrochronology (e.g. Curtis et al. 2020; Spada & Lanzafame 2020). Therefore, we believe our age estimations of all three targets are reliable.

In addition, we examined the kinematics of these three targets and determined that they are very likely thin disc stars. However, regarding TOI-2521, its age of ~10 Gry seems to conflict with the thin disc's age of ~8 Gyr. This discrepancy may indicate some inaccuracy in the isochrone fitting, and TOI-2521 may not be as old as 10 Gyr. However, it is important to note that stars also migrate and scatter, and there are old stars present in the thin disc as well. Therefore, we cannot draw a strong conclusion for a single star.

3.6 Asteroseismic analysis

No unambiguous solar-like oscillations could be detected for these three stars. We calculated their expected frequencies of maximum power ($\nu_{\rm max}$) using the spectroscopic $T_{\rm eff}$ and $\log g_*$ from Section 3.2 with the seismic scaling relation (Brown et al. 1991; Kjeldsen & Bedding 1995; Lund et al. 2016), yielding $\nu_{\rm max} \approx 853$ μHz for TOI-1608, $\nu_{\rm max} \approx 1221$ μHz for TOI-2336, and $\nu_{\rm max} \approx 968$ μHz for TOI-2521. Since these values are all greater than the Nyquist frequencies for 30-min (~278 μHz) and 10-min (~833 μHz) cadence light curves, only 2-min cadence data are suited for the detection of solar-like oscillations – which is only available for 1 sector for TOI-1608. We searched for oscillation signals using the LIGHTKURVE package (Lightkurve Collaboration 2018) and from manual inspection of the power density spectra of the light curves with the transit signals masked out, but could not identify any solar-like oscillations. Considering the TESS magnitudes of the stars (Campante et al. 2016), the fact that they were observed with TESS cameras 1 or 2 where background scattered light can be significant, and that clear rotational signals are evident in the photometry (at least for TOIs 1608 and 2521), indicating stellar surface activity that may suppress oscillation mode amplitudes (Chaplin et al. 2011), the non-detection is not entirely unexpected. Future *TESS* observations appended to the current coverage-limited light curves will be useful for searching for the oscillations of these stars.

4 ANALYSIS AND RESULTS

4.1 Joint RV and transit analysis

We jointly fit the detrended *TESS* light curves and RVs by utilizing the JULIET package (Espinoza et al. 2019). For TOI-2336, we also include the *LCOGT* light curves in the joint fitting. JULIET is a modelling tool for exoplanetary systems. It employs the BATMAN package (Kreidberg 2015) to build transit models and employs RADVEL (Fulton et al. 2018) to build RV models. It can fit both transit and RV data simultaneously by using bayesian inference with nested sampling with multiple choices of samplers. We used the sampler DYNESTY (Speagle 2020) in the following analyses.

In the modelling for the three systems, we set the priors based in a similar fashion. We set wide uniform priors for the transit epoch ($T_{0,b}$) and the orbital period (P_0) around the values from ExoFOP,[4] which are from the analysis by the *TESS* project. For the radius ratio ($p = R_b/R_*$) and the impact parameter ($b = a\cos i/R_*$), JULIET uses the approach described in Espinoza (2018) to fit the parametrizations r_1 and r_2 instead of fitting b and p directly. This parametrization allows us to efficiently sample the physically plausible zone in the (b,p) plane (i.e. $b < 1 + p$) by only simply uniformly sampling r_1 and r_2 between 0 and 1. Here we set uninformative uniform priors between 0 and 1 for r_1 and r_2. For the orbital eccentricity (e) and the argument of periapsis (ω_b), we chose to fit for the parameters $e\sin\omega_b$ and $e\cos\omega_b$. The uninformative priors should be uniform priors between -1 and 1 for these two parameters and JULIET will keep $e < 1$ when sampling. However, we found the fitting would be stuck if we allow e to be sampled very close to 1. Therefore, we set uniform priors between -0.7 and 0.7 for $e\sin\omega_b$ and $e\cos\omega_b$, which constrains $e < 0.99$. As such priors are significantly wider than the resulting posteriors and changing the width down to $(-0.1, 0.1)$ does not affect our final results, we think adopting such priors is essentially equivalent to using uninformative priors.

For the *TESS* light curves, because the *TESS* PDCSAP light curves have already been corrected for the light dilution, we fixed the dilution factor D as 1. However, the dilution correction may not be optimal due to the complex TESS background flux like scattered light. To make sure these possible errors would not influence our results, we adopted a Gaussian prior with a mean of 1 and a variance of 0.1 to fit the data and obtained consistent results. For TOI-2336 and TOI-2521, we also compared the transit depths by fitting the light curves of each individual sector independently, and the results are consistent. In addition, the contamination ratios of these 3 systems given by TICv8 on ExoFOP are all less than 0.05, indicating that the contamination is very small, so any errors in the contamination correction of the TESS PDCSAP light curves should be negligible. Therefore, we conclude that contamination or scattered light should not be an issue in the TESS light curves or affect our results. For TOI-2521, Since we detected a faint close companion (see Section 2.4.1), though we believe that it would only result in a radius error of less than 1 per cent, we still conducted additional testing to determine its potential impact. The companion is 3.94 magnitudes fainter than the primary star at 832 nm, representing ~ 2.7 per cent of its flux. Therefore, we fixed the dilution factor at 0.97 to fit the data, and the resulting radius ratio increased by less than 1σ. Therefore, we fixed the dilution factor as 1 for all three targets in our reported results.

We set a Gaussian prior with a zero mean and a small variance for the mean out-of-transit flux M because the light curves have

been detrended and normalized. We fitted an extra flux jitter term (σ) to account for additional noise and set a wide log-uniform prior based on the photometric uncertainties of the light curves. We adopted a quadratic limb-darkening law for the *TESS* light curves and fitted the limb-darkening parameters q_1 and q_2 (Kipping 2013) with uninformative priors between 0 and 1. For the *LCOGT* light curves of TOI-2336, we set similar priors for the dilution factor, mean out-of-transit flux, extra flux jitter term and limb-darkening parameters.

For the RV data, we fitted for the RV semi-amplitude (K) for each system with a systemic velocity (μ) for each instrument. We estimated rough values for these parameters from the data through visual inspection and set very wide and essentially uninformative uniform priors around these values. We fitted an extra RV jitter term to account for any additional systematics for each instrument. We set wide log-uniform priors for them according to the RV precision of each instrument. The RVs of NRES for TOI-1608 on 9th January 2022 (BJD = 2459588.661) and of CORALIE for TOI-2336 on 9th May 2021 (BJD = 2459343.687687) were observed in transit. However, based on the equation (1) in Triaud (2018), the predicted semi-amplitudes of the Rossiter–McLaughlin effect (McLaughlin 1924; Rossiter 1924) of these systems are both less than 50 m s^{-1}, which is less than the uncertainties of our RVs. Therefore, these RVs were not highly biased due to the transit and should not influence our RV modelling for the orbits.

We summarize the prior settings and the best-fitting values for each parameter in our modelling in Tables 4–6. We show the light curves with the best-fitting model in Figs 7 and 8, and show the RV data with the best-fitting model in Fig. 9.

We combine the parameters from the joint RV and transit modelling with the stellar parameters obtained in Section 3 to derive the physical parameters of the companions. The results are shown in Table 7.

4.2 Secondary eclipse

We conducted an analysis of the secondary eclipse signals in the *TESS* light curves. To prevent the removal of the secondary eclipse signal during detrending, we started by using *TESS* PDCSAP data and detrending the light curves. We masked out in-transit data as well as data predicted in the secondary eclipse based on the orbital parameters outlined in Section 4.1. To account for the uncertainties in the orbital parameters, we masked out an additional period of time equal to the transit duration before and after the predicted secondary eclipse. We then employed the PYTRANSIT package to fit the secondary eclipse. Our fitted parameters consisted of mid-transit time, orbital period, companion-to-star area ratio (equivalent to R_b^2/R_*^2), stellar density, impact parameter, companion-to-star flux ratio, $\sqrt{e}\sin\omega_b$, and $\sqrt{e}\cos\omega_b$ (e and ω_b refer to the orbital eccentricity and the argument of periapsis). We set Gaussian prior with the mean and the variance derived from the results of Section 4.1 for all fitted parameters except the companion-to-star flux ratio, for which we assigned a uniform prior between 0 and 1.

We found that the secondary eclipse signal of TOI-1608 is significant, with a companion-to-star flux ratio of 0.043 ± 0.007. The detrended light curve and the best-fitting model for this result are shown in Fig. 10. For TOI-2336 and TOI-2521, we found that their secondary eclipse signal is not significant and their flux ratio results are consistent with 0. Therefore, we only report the 3σ upper limit of the flux ratio, which is <0.092 for TOI-2336 and <0.072 for TOI-2521.

Table 4. Prior settings and the best-fitting values along with the 68 per cent credibility intervals in the final joint fit for TOI-1608. $\mathcal{N}(\mu\,,\,\sigma^2)$ means a normal prior with mean μ and standard deviation σ. $\mathcal{U}$(a, b) stands for a uniform prior ranging from a to b. $\mathcal{J}(a, b)$ stands for a Jeffrey's prior ranging from a to b.

Parameter	Prior	Best-fitting	Description
Companion's parameters			
P_b (d)	$\mathcal{U}$ (2.4, 2.6)	$2.47275^{+0.00004}_{-0.00004}$	Orbital period of TOI-1608b
$T_{0,b}$ (BJD)	$\mathcal{U}$ (2458791, 2458793)	$2458792.4599^{+0.0007}_{-0.0007}$	Mid-transit time of TOI-1608b
$r_{1,b}$	$\mathcal{U}$ (0, 1)	$0.952^{+0.003}_{-0.004}$	Parametrization for p and b
$r_{2,b}$	$\mathcal{U}$ (0, 1)	$0.057^{+0.002}_{-0.002}$	Parametrization for p and b
$e\sin\omega_b$	$\mathcal{U}$ (−0.7, 0.7)	$-0.02^{+0.03}_{-0.03}$	Parametrization for e and ω_b
$e\cos\omega_b$	$\mathcal{U}$ (−0.7, 0.7)	$0.02^{+0.03}_{-0.03}$	Parametrization for e and ω_b
TESS photometry parameters			
$D_{\text{TESS-S18}}$	Fixed	1	*TESS* photometric dilution factor
$M_{\text{TESS-S18}}$	$\mathcal{N}$ (0, 0.1²)	$0.0000004^{+0.000003}_{-0.000003}$	Mean out-of-transit flux of *TESS* photometry
$\sigma_{\text{TESS-S18}}$ (ppm)	$\mathcal{J}$ (0.1, 1000)	239^{+3}_{-3}	*TESS* additive photometric jitter term
$q_{1,\text{ TESS-S18}}$	$\mathcal{U}$ (0, 1)	$0.12^{+0.12}_{-0.08}$	Quadratic limb darkening coefficient
$q_{2,\text{ TESS-S18}}$	$\mathcal{U}$ (0, 1)	$0.48^{+0.30}_{-0.32}$	Quadratic limb darkening coefficient
Stellar parameters			
ρ_* (kg m^{-3})	$\mathcal{J}$ (10, 1000)	224^{+27}_{-21}	Stellar density
RV parameters			
K_b (m s^{-1})	$\mathcal{U}$ (0, 20 000)	10649^{+232}_{-216}	RV semi-amplitude of TOI-1608b
NRES RV parameters			
μ_{NRES} (m s^{-1})	$\mathcal{U}$ (70 000, 100 000)	82204^{+281}_{-283}	Systemic velocity for *NRES*
σ_{NRES} (m s^{-1})	$\mathcal{J}$ (1, 10 000)	542^{+139}_{-103}	Extra jitter term for *NRES*

Then we used the obtained results to estimate the effective temperature of the companions. According to Charbonneau et al. (2005), the flux ratio should be

$$\frac{F_b}{F_*} = \frac{\int F_b(\lambda)S(\lambda)\lambda\,\mathrm{d}\lambda}{\int F_*(\lambda)S(\lambda)\lambda\,\mathrm{d}\lambda}, \tag{1}$$

where $S(\lambda)$ is the *TESS* spectral response function, $F_b(\lambda)$ and $F_*(\lambda)$ represent the companion's and stellar surface fluxes as a function of the wavelength, respectively. For simplicity, we assumed blackbody spectra for both the companion and the star and neglected the reflected light, meaning that the albedo is 0. Combining the *TESS* spectral response function[5] and the stellar effective temperature from Table 1, we estimated the effective temperature of the companions as follows: TOI-1608: 2983 ± 90 K, TOI-2336: <3566 K, and TOI-2521: <3143 K. When assuming that the blackbody radiation of these companions is balanced with their incident flux, the corresponding equilibrium temperatures would be about 2081, 1509, and 1474 K, respectively. These values are all lower than the estimated effective temperature and upper limits, which is expected since these three targets are brown dwarfs or low-mass stars.

For TOI-1608, as its secondary eclipse signal is significant, we may use this signal to independently constrain its eccentricity. Although we used e and ω_b from the transit to predict the time of the secondary eclipse when we detrended the light curves, the additional part we masked out ensures our results can remain independent with the e and ω_b from transit. To constrain the eccentricity, we set a uniform prior from −1 to 1 for $\sqrt{e}\sin\omega_b$, and $\sqrt{e}\cos\omega_b$, kept other priors, and fitted the light curves. However, we found the secondary eclipse did not provide strong constraints on e and ω_b, as the posterior of

e was wide and consistent with a near zero e, consistent with our results from the joint fit listed in Table 7.

5 DISCUSSION

5.1 Mass-radius relation and Inflation

We compare TOI-1608b, TOI-2336b, and TOI-2521b with the models from Baraffe et al. (2015) and Phillips et al. (2020) in the mass-radius diagram, which is shown in Fig. 11. For the following analysis, we also build a sample of transiting companions with a mass between $13\,M_J$ and $150\,M_J$. We use the sample compiled by Grieves et al. (2021) and add NGTS-19b (Acton et al. 2021), TOI-1278 B (Artigau et al. 2021), TOI-2119b (Cañas et al. 2022; Carmichael et al. 2022), TIC-320687387 B (Gill et al. 2022), TOI-629b, TOI-1982b, and TOI-2543b (Psaridi et al. 2022). We call them the 'previous transiting BDs and low-mass stars sample' in the following text, and we also plot this sample in Fig. 11. The sample and the codes for this figure are available on Github[6] According to the plotted model isochrones, all of our three targets seem to be younger than 0.5 *Gyr*. This is much younger than the ages we obtained in Section 3 for the primary stars. For TOI-1608 and TOI-2336, if we adopt a very low age limit of 1 *Gyr* for these systems, the predicted radii from the model isochrones would be $1.06\,R_J$ and $0.90\,R_J$, respectively, both of which are about 3σ smaller than the measured values from our joint transit and RV analyses. For TOI-2521, if we adopt a very low age limit of 5 *Gyr* for the system, the predicted radius would be $0.84\,R_J$, which is 4σ smaller than our measured value. Therefore, TOI-1608b, TOI-2336b, and TOI-2521b should be all inflated.

[5]https://heasarc.gsfc.nasa.gov/docs/tess/the-tess-space-telescope.html

[6]https://github.com/Ssealevel/Codes_TOI-1608_2336_2521

Table 5. Similar to Table 4 but for TOI-2336.

Parameter	Prior	Best-fitting	Description
Companion's parameters			
P_b (days)	$\mathcal{U}\,(7.6, 7.8)$	$7.711978^{+0.000013}_{-0.000013}$	Orbital period of TOI-2336b
$T_{0,b}$ (BJD)	$\mathcal{U}\,(2459\,358, 2459\,360)$	$2459359.0493^{+0.0006}_{-0.0006}$	Mid-transit time of TOI-2336b
$r_{1,b}$	$\mathcal{U}\,(0, 1)$	$0.874^{+0.013}_{-0.014}$	Parametrization for p and b
$r_{2,b}$	$\mathcal{U}\,(0, 1)$	$0.0592^{+0.0008}_{-0.0007}$	Parametrization for p and b
$e\sin\omega_b$	$\mathcal{U}\,(-0.7, 0.7)$	$-0.007^{+0.008}_{-0.007}$	Parametrization for e and ω_b
$e\cos\omega_b$	$\mathcal{U}\,(-0.7, 0.7)$	$0.006^{+0.003}_{-0.003}$	Parametrization for e and ω_b
TESS photometry parameters			
$D_{\text{TESS-S11}}$	Fixed	1	*TESS* photometric dilution factor
$D_{\text{TESS-S38}}$	Fixed	1	
$M_{\text{TESS-S11}}$	$\mathcal{N}\,(0, 0.1^2)$	$0.0000009^{+0.000009}_{-0.000009}$	Mean out-of-transit flux of *TESS* photometry
$M_{\text{TESS-S38}}$	$\mathcal{N}\,(0, 0.1^2)$	$-0.000001^{+0.000008}_{-0.000008}$	
$\sigma_{\text{TESS-S11}}$ (ppm)	$\mathcal{J}\,(1, 10\,000)$	12^{+35}_{-10}	*TESS* additive photometric jitter term
$\sigma_{\text{TESS-S38}}$ (ppm)	$\mathcal{J}\,(1, 10\,000)$	117^{+28}_{-42}	
$q_{1,\text{TESS-S11}}$	$\mathcal{U}\,(0, 1)$	$0.19^{+0.12}_{-0.09}$	Quadratic limb darkening coefficient
$q_{1,\text{TESS-S38}}$	$\mathcal{U}\,(0, 1)$	$0.12^{+0.07}_{-0.06}$	
$q_{2,\text{TESS-S11}}$	$\mathcal{U}\,(0, 1)$	$0.32^{+0.31}_{-0.20}$	Quadratic limb darkening coefficient
$q_{2,\text{TESS-S38}}$	$\mathcal{U}\,(0, 1)$	$0.56^{+0.27}_{-0.32}$	
LCOGT photometry parameters			
D_{LCOGT}	Fixed	1	*LCOGT* photometric dilution factor
M_{LCOGT}	$\mathcal{N}\,(0, 0.1^2)$	$0.00015^{+0.00009}_{-0.00009}$	Mean out-of-transit flux of *LCOGT* photometry
σ_{LCOGT} (ppm)	$\mathcal{J}\,(1, 10\,000)$	1179^{+62}_{-62}	*LCOGT* additive photometric jitter term
$q_{1,\text{LCOGT}}$	$\mathcal{U}\,(0, 1)$	$0.02^{+0.04}_{-0.02}$	Quadratic limb darkening coefficient
$q_{2,\text{LCOGT}}$	$\mathcal{U}\,(0, 1)$	$0.54^{+0.28}_{-0.32}$	Quadratic limb darkening coefficient
Stellar parameters			
ρ_* (kg m^{-3})	$\mathcal{J}\,(10, 1000)$	246^{+38}_{-31}	Stellar density
RV parameters			
K_b (m s^{-1})	$\mathcal{U}\,(0, 20\,000)$	5549^{+37}_{-39}	RV semi-amplitude of TOI-2336b
NRESRV parameters			
μ_{NRES} (m s^{-1})	$\mathcal{U}\,(20\,000, 40\,000)$	33707^{+327}_{-314}	Systemic velocity for *NRES*
σ_{NRES} (m s^{-1})	$\mathcal{J}\,(0.1, 10\,000)$	1586^{+264}_{-205}	Extra jitter term for *NRES*
CHIRONRV parameters			
μ_{CHIRON} (m s^{-1})	$\mathcal{U}\,(20\,000, 40\,000)$	30288^{+52}_{-50}	Systemic velocity for *CHIRON*
σ_{CHIRON} (m s^{-1})	$\mathcal{J}\,(0.1, 10\,000)$	$4.7^{+27.3}_{-4.2}$	Extra jitter term for *CHIRON*
CORALIERV parameters			
μ_{CORALIE} (m s^{-1})	$\mathcal{U}\,(20\,000, 40\,000)$	32432^{+36}_{-34}	Systemic velocity for *CORALIE*
σ_{CORALIE} (m s^{-1})	$\mathcal{J}\,(0.1, 10\,000)$	104^{+40}_{-33}	Extra jitter term for *CORALIE*

The radius inflation of hot Jupiters has been observed and characterized in multiple previous studies (e.g. Bouchy et al. 2011; Weiss et al. 2013), and the stellar incident flux clearly plays an important role in shaping the sizes of these giant planets. Weiss et al. (2013) obtained an empirical relation for the inflation of planets heavier than $150\,\text{M}_\oplus$ $(0.47\,M_J)$

$$\frac{R_p}{\text{R}_\oplus} = 2.5 \left(\frac{M_p}{\text{M}_\oplus}\right)^{-0.039} \left(\frac{F}{\text{erg s}^{-1}\,\text{cm}^{-2}}\right)^{0.094}. \tag{2}$$

However, for brown dwarf companions, previous research concluded that the stellar irradiation would not affect their radii as much as observed for the hot Jupiters (e.g. Bouchy et al. 2011). To compare the dependence on the incident flux for hot Jupiters, brown dwarfs,

and low-mass stars, we used the 'previous transiting BDs and low-mass stars sample' and fitted a similar power-low relation to that of Weiss et al. (2013) as

$$\frac{R_p}{R_J} = C \left(\frac{M_p}{M_J}\right)^\alpha \left(\frac{F}{\text{F}_\oplus}\right)^\beta. \tag{3}$$

We fitted this relation for brown dwarfs and low-mass stars separately with a cut-off at $80\,M_J$ (Baraffe et al. 2002) to distinguish them. For both sets of samples, we calculated their time-averaged incident flux using the equation

$$F = \sigma_{\text{sb}} T_{\text{eff}}^4 \left(\frac{R_*}{a}\right)^2 \sqrt{\frac{1}{1-e^2}}, \tag{4}$$
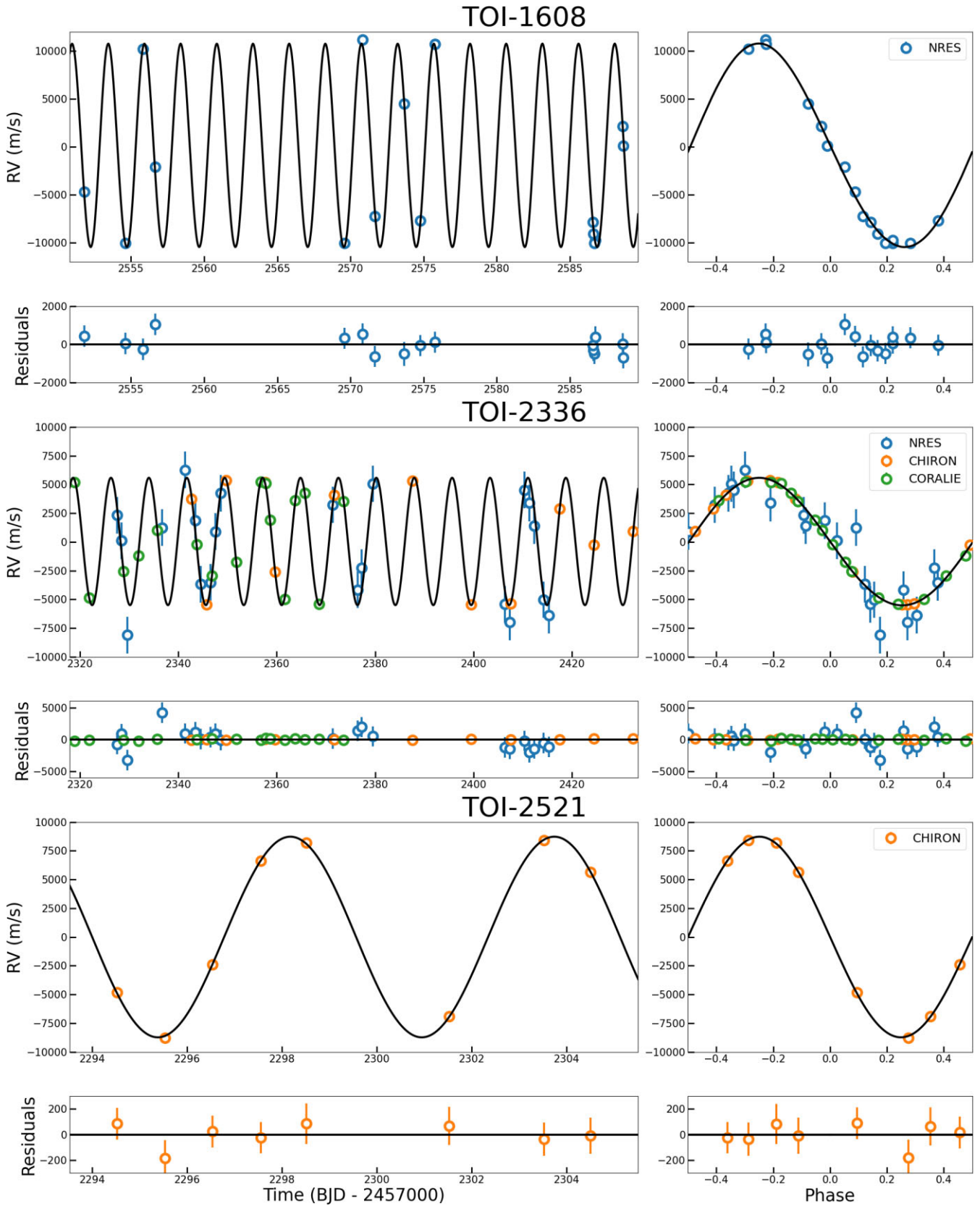
Figure 9. The RVs of TOI-1608, TOI-2336, and TOI-2521. The black line is the best-fitting model obtained by JULIET. The error bars are the quadrature sum of the instrument jitter term and the measurement uncertainties for all RVs. The left row is the RVs as a function of time and the right row is the phase-folded RVs.

Table 6. Similar to Table 4 but for TOI-2521.

Parameter	Prior	Best-fitting	Description
Companion's parameters			
P_b (d)	$\mathcal{U}$ (5.5, 5.6)	$5.563060^{+0.000007}_{-0.000007}$	Orbital period of TOI-2521b
$T_{0,b}$ (BJD)	$\mathcal{U}$ (2459 226, 2459 228)	$2459227.2466^{+0.0007}_{-0.0007}$	Mid-transit time of TOI-2521b
$r_{1,b}$	$\mathcal{U}$ (0, 1)	$0.71^{+0.07}_{-0.13}$	Parametrization for p and b
$r_{2,b}$	$\mathcal{U}$ (0, 1)	$0.0598^{+0.0011}_{-0.0013}$	Parametrization for p and b
$e\sin\omega_b$	$\mathcal{U}$ (−0.7, 0.7)	$0.003^{+0.007}_{-0.007}$	Parametrization for e and ω_b
$e\cos\omega_b$	$\mathcal{U}$ (−0.7, 0.7)	$0.0003^{+0.004}_{-0.004}$	Parametrization for e and ω_b
TESS photometry parameters			
$D_{\mathrm{TESS\text{-}S6}}$	Fixed	1	*TESS* photometric dilution factor
$D_{\mathrm{TESS\text{-}S33}}$	Fixed	1	
$M_{\mathrm{TESS\text{-}S6}}$	$\mathcal{N}$ (0, 0.1²)	$-0.000004^{+0.000012}_{-0.000012}$	Mean out-of-transit flux of *TESS* photometry
$M_{\mathrm{TESS\text{-}S33}}$	$\mathcal{N}$ (0, 0.1²)	$-0.000004^{+0.000011}_{-0.000011}$	
$\sigma_{\mathrm{TESS\text{-}S6}}$ (ppm)	$\mathcal{J}$ (0.001, 10)	$0.25^{+2.38}_{-0.24}$	*TESS* additive photometric jitter term
$\sigma_{\mathrm{TESS\text{-}S33}}$ (ppm)	$\mathcal{J}$ (0.001, 10)	$0.12^{+1.99}_{-0.11}$	
$q_{1,\mathrm{TESS\text{-}S6}}$	$\mathcal{U}$ (0, 1)	$0.15^{+0.11}_{-0.07}$	Quadratic limb darkening coefficient
$q_{1,\mathrm{TESS\text{-}S33}}$	$\mathcal{U}$ (0, 1)	$0.16^{+0.11}_{-0.08}$	
$q_{2,\mathrm{TESS\text{-}S6}}$	$\mathcal{U}$ (0, 1)	$0.40^{+0.37}_{-0.28}$	Quadratic limb darkening coefficient
$q_{2,\mathrm{TESS\text{-}S33}}$	$\mathcal{U}$ (0, 1)	$0.31^{+0.27}_{-0.20}$	
Stellar parameters			
ρ_* (kg m⁻³)	$\mathcal{J}$ (10, 1000)	269^{+115}_{-77}	Stellar density
RV parameters			
K_b (m s⁻¹)	$\mathcal{U}$ (0, 20 000)	8725^{+73}_{-59}	RV semi-amplitude of TOI-2521b
CHIRONRV parameters			
μ_{CHIRON} (m s⁻¹)	$\mathcal{U}$ (−40 000, −20 000)	-31334^{+49}_{-48}	Systemic velocity for *CHIRON*
σ_{CHIRON} (m s⁻¹)	$\mathcal{J}$ (0.1, 1000)	113^{+96}_{-53}	Extra jitter term for *CHIRON*

**Table 7.** Physical parameters for TOI-1608b, TOI-2336b, and TOI-2521b.

Parameter	TOI-1608	TOI-2336	TOI-2521	Description
P (d)	$2.47275^{+0.00004}_{-0.00004}$	$7.711978^{+0.000013}_{-0.000013}$	$5.563060^{+0.000007}_{-0.000007}$	Orbital period
R_b/R_*	$0.0574^{+0.0020}_{-0.0016}$	$0.0592^{+0.0008}_{-0.0007}$	$0.0598^{+0.0011}_{-0.0007}$	Companion radius in units of stellar radius
R_b (R_J)	$1.21^{+0.06}_{-0.06}$	$1.05^{+0.04}_{-0.04}$	$1.01^{+0.04}_{-0.04}$	Companion radius
M_b (M_J)	$90.7^{+3.7}_{-3.7}$	$69.9^{+2.3}_{-2.3}$	$77.5^{+3.3}_{-3.3}$	Companion mass
ρ_b (g cm⁻³)	$63.7^{+10.3}_{-9.1}$	$75.0^{+8.9}_{-7.9}$	$92.8^{+12.3}_{-10.7}$	Companion density
b	$0.929^{+0.004}_{-0.006}$	$0.810^{+0.019}_{-0.021}$	$0.56^{+0.11}_{-0.10}$	Impact parameter
a/R_*	$4.17^{+0.16}_{-0.13}$	$9.18^{+0.44}_{-0.40}$	$7.60^{+0.96}_{-0.81}$	Semi-major axis in units of stellar radius
a (au)	$0.0419^{+0.0022}_{-0.0021}$	$0.0777^{+0.0046}_{-0.0042}$	$0.0615^{+0.0079}_{-0.0067}$	Semimajor axis
i (deg)	$77.1^{+0.5}_{-0.5}$	$84.9^{+0.4}_{-0.4}$	$85.8^{+1.8}_{-1.4}$	Inclination angle
e	$0.041^{+0.024}_{-0.019}$	$0.010^{+0.006}_{-0.005}$	$<0.035^a$	Eccentricity
F ($F_\oplus$)	3155^{+289}_{-278}	846^{+92}_{-86}	721^{+185}_{-153}	Insolation flux relative to the Earth

^{a}Here, we report the upper limits at the 99 per cent confidence level.

where σ_{sb} is the Stefan–Boltzmann constant. In the following analyses we excluded from the samples objects with precision on the radius or mass that is poorer than 30 per cent. We also excluded RIK 72b because it is a very young brown dwarf (David et al. 2019) and probably still in the process of initial contraction after its formation. Finally, we have 34 brown dwarfs and 25 low-mass stars in our fitting. We used EMCEE (Foreman-Mackey et al. 2013) to perform a Markov chain Monte Carlo (MCMC) fitting for each sample. We set uniform priors between −5 and 5 for α and β and a log-uniform prior between 10^{-5} and 10^5 for C. The MCMC posteriors are shown in Fig. 12 and the best-fitting values are listed in Table 8. The best-fitting relation for the brown dwarfs ($13\,M_J \sim 80\,M_J$) is

$$\frac{R_p}{R_J} = 1.11 \left(\frac{M_p}{M_J}\right)^{-0.052} \left(\frac{F}{\mathrm{F}_\oplus}\right)^{0.009}, \tag{5}$$
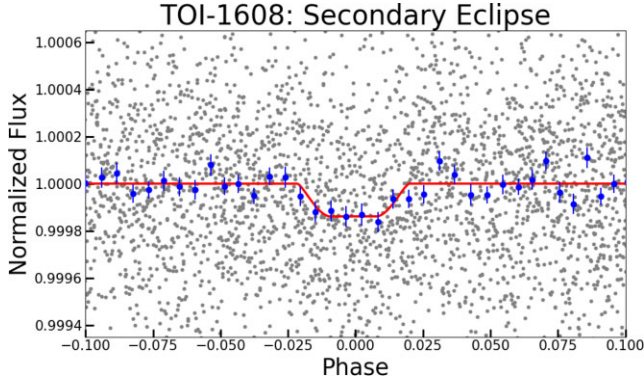
Figure 10. The TESS light curves near the secondary eclipse of TOI-1608. The detrended TESS PDCSAP data, described in Section 4.2, are represented by gray dots and the binned data are in blue. The red line represents the best-fitting secondary eclipse model obtained by PYTRANSIT.
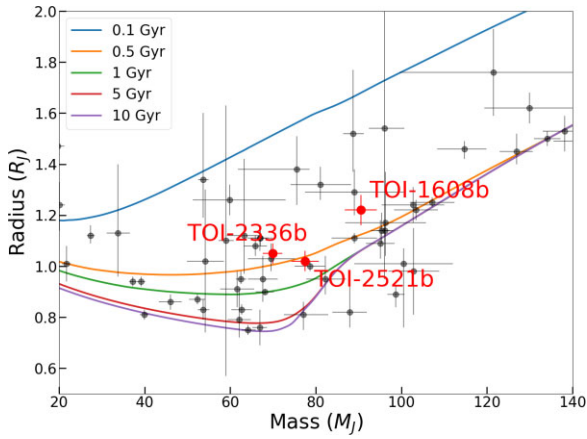

Figure 11. Radius–mass diagram for the transiting brown dwarfs and low-mass stars. The black dots are the 'previous transiting BDs and low-mass stars sample,' and the red dots are the three targets in this work. The isochrones of 0.1, 0.5, 1, 5, and 10 Gyr at solar metallicity from Baraffe et al. (2015) and Phillips et al. (2020) models are shown as lines with different colours. The sample and codes for generating this figure are available on https://github.com/Ssealevel/Codes_TOI-1608_2336_2521.

and the relation for the low-mass stars ($80 M_J \sim 150 M_J$) is

$$\frac{R_p}{R_J} = 0.021 \left(\frac{M_p}{M_J}\right)^{0.86} \left(\frac{F}{F_\oplus}\right)^{0.019}. \tag{6}$$

In Fig. 13, we show the sample of transiting low-mass companions with mass around $13 M_J \sim 150 M_J$ as well as the sample of known hot Jupiters with the published values for the radius and the incident flux with a precision better than 50 per cent. The empirical relations for different types of objects are shown as different lines. Comparing these results, we find that the mass–radius relations for the three kinds of objects are different. The mass dependence for brown dwarfs and low-mass stars from our fits is consistent with Chen & Kipping (2017). Besides, the power-law indices for incident flux in the mass–radius relation for brown dwarfs and low-mass stars are significantly lower than that for hot Jupiters, which confirms that brown dwarfs are less affected by stellar irradiation (e.g. Bouchy et al. 2011). However, the best-fitting indices for incident flux for brown dwarfs and low-mass stars are not consistent with zero, which suggests that the effect on the size of these objects by the stellar irradiation is perhaps not totally negligible. Naively, one would speculate that objects with
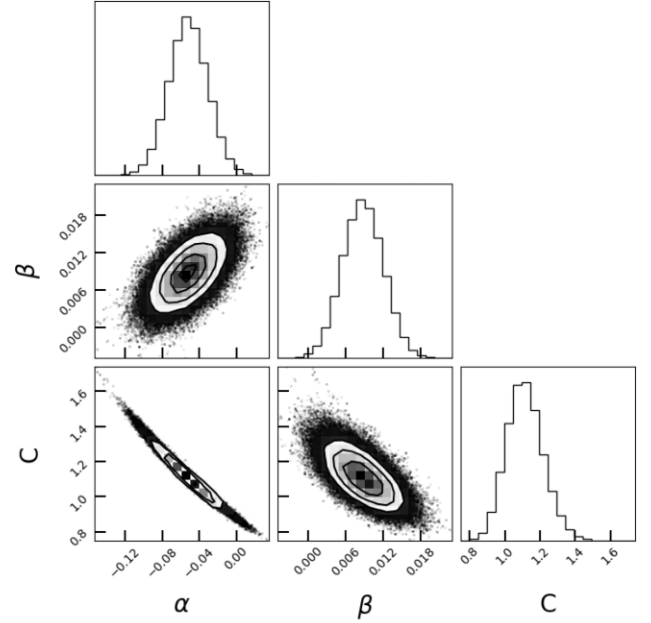
(a) Brown dwarfs
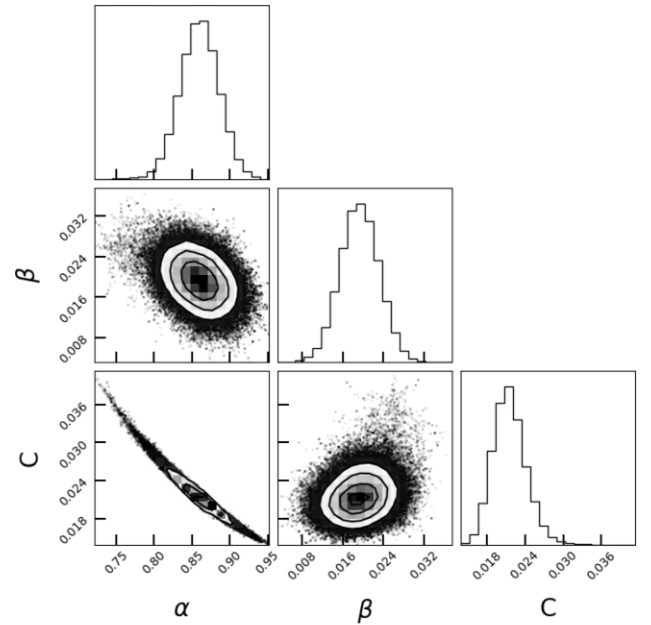
(b) Low mass stars

Figure 12. The posterior distribution of the MCMC fitting of equation (3) for brown dwarfs and low-mass stars. C is the normalization parameter, α is the power-law index for mass, and β is the power-law index for incident flux. The corresponding results of these parameters are listed in Table 8.

higher densities or higher surface gravity should be more difficult to inflate via external irradiation. Since brown dwarfs have higher densities than low-mass stars on average (Baraffe et al. 2003; Baraffe, Chabrier & Barman 2008) (also see fig. 8 in Persson et al. 2019), it is consistent with the expectation that the brown dwarfs' radii have a weaker dependence on the incident flux than the low-mass stars' (a smaller power-law index). Future studies with a larger and better characterized sample of low-mass objects may reveal more on
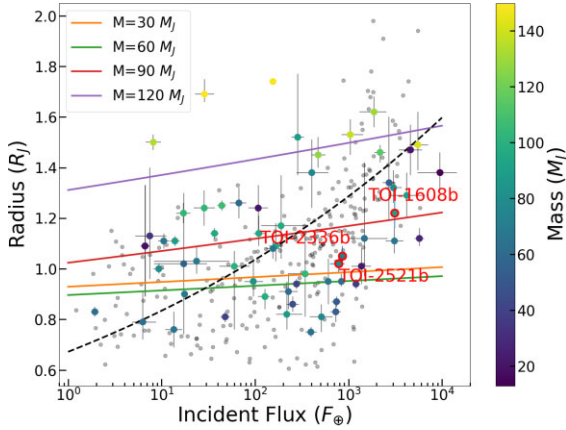
Figure 13. The incident flux received by the companions versus their radii. Dots with different colours are the 'previous transiting BDs and low-mass stars sample,' and the colour scale represents the mass of these companions. The dots with red outlines are the three targets in this work and the grey dots in the background are hot Jupiters. Here, we only show brown dwarfs and low-mass stars with mass and radius measured with a precision better than 30 per cent and hot Jupiters with radius and incident flux with a precision better than 50 per cent. Equations (5) and (6) are plotted in solid lines for two different selected masses in each mass range, and the dashed line presents the Weiss et al. (2013) relation for hot Jupiters with $1\,M_J$. The sample and codes for generating this figure are available on https://github.com/Ssealevel/Codes_TOI-1608_2336_2521.

Table 8. MCMC fitting results of equation (3) for brown dwarfs and low-mass stars.

Parameter	Brown dwarfs	Low-mass stars
α	$-0.052^{+0.021}_{-0.021}$	$0.860^{+0.025}_{-0.026}$
β	$0.009^{+0.003}_{-0.003}$	$0.019^{+0.004}_{-0.004}$
C	$1.11^{+0.11}_{-0.10}$	$0.021^{+0.002}_{-0.002}$

this potential difference between these two populations. Finally, we caution that the radii of brown dwarfs and low-mass stars can change considerably as they age (as can be seen in the isochrones in Fig. 11). For example, since the radii decrease with age, and irradiation is higher closer to the star where tidal effects are also stronger, if tides are strong enough to cause orbital decay and destruction of close-in objects within the main sequence lifetime of the host stars, then this may result in closer-in brown dwarfs being systematically younger and with larger radii than farther out objects. This may mimic a trend with irradiation. However, due to the lack of samples with accurate ages, we were unable to consider the dependence on age in this discussion. More samples with accurate age estimates and a more comprehensive analysis are needed in future works.

5.2 Tidal effects

Tidal effects are important in the evolution of close binary systems. There are several tidal effects to consider for binary systems with a relatively high-mass ratio like the three cases here: tidal circularization, orbital decay, and spin-orbit synchronization. We discuss tidal circularization in Section 5.2.1. In Section 5.2.2, we discuss spin-orbit synchronization as well as the fast rotation of TOI-1608 and TOI-2521. Finally, we discuss the orbital decay in Section 5.2.3.

5.2.1 Tidal circularization

The tidal circularization effect is where the tidal force damps the eccentricity of the orbit. We examine the orbital circularization time-scale

$$\tau_e = \frac{e}{|\mathrm{d}e/\mathrm{d}t|} \tag{7}$$

of the three targets by using the equation from Jackson et al. (2008):

$$\frac{1}{e}\frac{\mathrm{d}e}{\mathrm{d}t} = -\left[\frac{63}{4}(GM_*^3)^{1/2}\frac{R_p^5}{Q_pM_p} + \frac{171}{16}(G/M_*)^{1/2}\frac{R_*^5M_p}{Q_*}\right]a^{-13/2}, \tag{8}$$

where Q_p is the modified quality factor of the companion and Q_* is the modified quality factor of the host star. The quality factor is impossible to measure precisely. For brown dwarf companions, this value is usually adopted as $Q_p = Q_* = 10^6$ at face value. Under this assumption, the orbital circularization time-scales are 2.13, 373, and 41.3 Myr for TOI-1608, TOI-2336, and TOI-2521, respectively. Compared to the stellar ages derived in Section 3, the orbital circularization time-scales are much smaller, which means it is very likely that the orbits have been circularized. This is consistent with the measured low eccentricities of these three systems.

5.2.2 Spin-orbit synchronization

Dissipative tidal interactions alter both the orbital periods and the rotation periods of the host star and may lead to spin-orbit synchronization (Goldreich & Soter 1966). For TOI-1608 and TOI-2521, as discussed in Section 3.5, we have determined that they are old stars, but their fast rotations appear inconsistent with their age. However, since their rotation periods (see Table 1) are very close to their companion orbit periods (see Table 7), the fast rotation might be explained by spin-orbit synchronization. To verify this scenario, we adopted the tidal model in Hut (1981) and calculated the ratio of orbital and rotational angular momentum at the stable equilibrium configuration (α) for these two systems. Here the equilibrium configuration means coplanarity (the spin axis of the two stars and the orbit are aligned), circularity (of the orbit), and spin-orbit synchronization of a binary system. In summary, Hut (1981) suggested that such an equilibrium state is stable only when $\alpha > 3$. When $\alpha < 3$ and $\alpha - 3 \ll 1$, the system will reach the circularity relatively quickly and take much more time to reach the spin-orbit synchronization. When $\alpha \sim 7$, the system will reach both circularity and synchronization roughly at the same time. When $\alpha \gg 7$, the system will reach synchronization much more quickly than it will reach circularity. Assuming the moment of inertia $I = 0.07M_*R_*^2$ as the sun[7], we obtained $\alpha = 14$ for TOI-1608 and $\alpha = 60$ for TOI-2521, which suggests that these systems can reach spin-orbit synchronization and that the spin-orbit synchronization will take less time than tidal circularization. In Section 5.2.1, we found these two systems are very likely to be circularized. Therefore, it is reasonable to suggest that these two systems have been spin-orbit synchronized, which led to the fast rotation of the host stars.

We also estimated the synchronization time-scales for these two systems. Here we adopted the equations (2) and (3) in Albrecht et al. (2012), which are based on the formulae from Zahn (1977) and are calibrated with observations of binary stars:

---

[7]https://nssdc.gsfc.nasa.gov/planetary/factsheet/sunfact.html

$$\frac{1}{\tau_{\rm CE}} = \frac{1}{10 \times 10^9 \,{\rm yr}} q^2 \left(\frac{a/R_*}{40}\right)^{-6}, \qquad (9)$$

$$\frac{1}{\tau_{\rm RA}} = \frac{1}{0.25 \times 5 \times 10^9 \,{\rm yr}} q^2 (1+q)^{5/6} \left(\frac{a/R_*}{6}\right)^{-17/2}, \qquad (10)$$

where $\tau_{\rm CE}$ and $\tau_{\rm RA}$ are the synchronization time-scales for cool stars with convective envelopes and hot stars with radiative envelopes, respectively, and q is the companion-to-star mass ratio. In Albrecht et al. (2012), they adopted $T_{\rm eff} = 6250$ K as the transition between stars with radiative and convective envelopes. As the effective temperatures of TOI-1608 and TOI-2521 are all smaller than 6250 K, we assumed convective envelopes and obtained $\tau_{\rm CE} = 2.9$ Myr for TOI-1608 and $\tau_{\rm CE} = 77$ Myr for TOI-2521. These time-scales are much smaller than our estimated ages. Therefore, we conclude that TOI-1608 and TOI-2521 are very likely old stars, and their fast rotations result from spin-orbit synchronization.

For TOI-2336, the rotation period is 4.2 ± 0.5 d, which is 7σ smaller than the orbital period of 7.71 d. This significant difference makes spin-orbit synchronization unlikely. However, if the orbital period were the second harmonics of 8.4 ± 1.0 d, synchronization would become a possibility. Nevertheless, considering that the $v\sin i$ derived from the spectra is faster than the velocity inferred by the rotation period of 4.2 d (as discussed in Section 3.4), the likelihood of an $\sim$8.4-d period is low. Therefore, it is unlikely for this system to have reached spin-orbit synchronization. In addition, we used equation (10) to calculate its synchronization time-scales and obtained $\tau_{\rm RA} = 1.9 \times 10^4$ Gyr, which is consistent with the notion that TOI-2336 has not yet reached synchronization.

5.2.3 Orbital decay

When the orbital period is shorter than the stellar rotation period, the semimajor axis of the companion's orbit will shrink and the companion will experience orbital tidal decay. According to the equation in Patra et al. (2017) derived from Goldreich & Soter (1966), the tidal decay time-scale is

$$\tau_P = \frac{P}{|{\rm d}P/{\rm d}t|} = \frac{2Q_*}{27\pi} \left(\frac{M_*}{M_p}\right)\left(\frac{a}{R_*}\right)^5 P, \qquad (11)$$

where P is the orbital period. For evolved host stars, the decay will become faster as the radius of the host star increases. For TOI-2336, since its orbital period is larger than the stellar rotation period, its orbit should not experience decay. For TOI-1608 and 2521, though we conclude in Section 5.2.2 that TOI-1608 and TOI-2521 have likely achieved spin-orbit synchronization, we still investigated their orbital decay time-scales to gain insight into how rapidly their orbit would decay in case they had not achieved synchronization yet. Using equation (11) and adopting $Q_* = 10^6$, we obtained 3.05 and 73.2 Myr for TOI-1608 and TOI-2521, respectively. The orbital decay time-scale of TOI-1608b is similar to that of WASP-12b, whose orbital decay has been reported (Maciejewski et al. 2016; Patra et al. 2017; Yee et al. 2020; Wong et al. 2022). Based on equation (11), we calculated the decay rate of the orbital period to be $\sim$70 ms yr^{-1}, which only induces a difference of $\sim$4.6 ms in our *TESS* observation. As the uncertainty on the orbital period in our analysis is 3.5 s, the orbital decay of TOI-1608b is not detectable in the *TESS* data gathered so far. Nevertheless, the orbital decay of WASP-12b was measured after being observed for a decade. Therefore, if TOI-1608 have not been spin-orbit synchronized, we might have a chance to observe their orbital decay in future observations (e.g. in *TESS* Extended Missions). On the other hand, if TOI-1608 and 2521 have
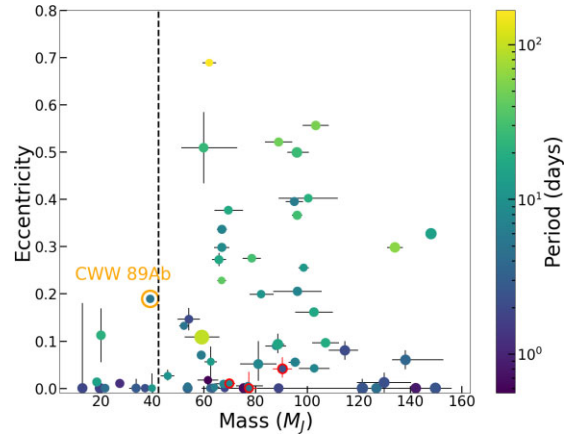
Figure 14. The eccentricities of transiting companions with a mass between 13 and 150 M_J as a function of mass. The dots with different colours are the 'previous transiting BDs and low-mass stars sample' and our targets are circled in red. The dots are sized by the radii of the companions and the colour shows their orbital periods. The dashed line is the mass threshold at 42.5 M_J proposed by Ma & Ge (2014) separating two different brown dwarf populations. We denoted CWW 89Ab, a possible outlier in the low-mass brown dwarf population, with the orange circle and presented a short discussion in Section 5.3. The sample and codes for generating this figure are available on https://github.com/Ssealevel/Codes_TOI-1608_2336_2521.

indeed reached tidal spin-orbit synchronization, magnetic braking could then cause further orbital decay with different time-scales (e.g. Barker & Ogilvie 2009; Li & Winn 2016; Benbakoura et al. 2019).

5.3 Eccentricity

In Section 5.2, we showed the low eccentricities of TOI-1608b, TOI-2336b, and TOI-2521b are consistent with their relatively short tidal circularization time-scales. Here, we put these three system in a broader context by comparing their eccentricities with previous statistical results. In Ma & Ge (2014), they analysed brown dwarf companions and found different eccentricity distributions for brown dwarfs below and above 42.5 M_J. The eccentricity distribution of low-mass brown dwarf companions is consistent with that of massive planets, while the high-mass brown dwarf companions show more diversity in their eccentricity distribution, more consistent with binaries. We show the eccentricities of the 'previous transiting BDs and low-mass stars sample' as well as our targets in Fig. 14. More diverse eccentricities can be seen in the region above 42.5 M_J. All our targets are in the high-mass region, but all have very low eccentricities in contrast to the majority of the high-mass brown dwarfs. We can see that companions with smaller periods tend to have lower eccentricities. This trend was also found by Ma & Ge (2014), and they suggested that this is caused by tidal circularization. All of our targets have relatively small orbital periods and thus are consistent with their observed trend.

In addition, the possible outlier in the low-mass region of Fig. 14 is CWW 89Ab (Curtis et al. 2016; Nowak et al. 2017; Beatty et al. 2018), which is denoted by the orange circle. This system has an M dwarf companion on a wide orbit, which might help explain its architecture and provide insight into the formation and migration of brown dwarf companions.

As all our targets are companions orbiting aged stars, we also compared the eccentricities with the sample of hot Jupiters from Grunblatt et al. (2018). They analysed a sample of hot Jupiters around 419 dwarf stars and 136 giant stars with planetary radii $R_p > 0.4 R_J$

and orbital periods between 4.5 and 30 d. They found that for the giant planets with short orbital periods, the ones orbiting evolved stars tend to have higher eccentricities (with a median eccentricity of $e \approx 0.152$) than the giant planets orbiting main-sequence dwarfs (with a median eccentricity of $e \approx 0.056$). They suggest that this may be caused by the increasing tidal effect of the evolved stars as their radii increase post-main-sequence: the planets with shorter tidal circularization time-scales would also have relatively short tidal decay time-scales and thus be engulfed. As a result, we would observe more planets with high eccentricities. All of our targets have eccentricities that are significantly lower than the median eccentricity of $e \approx 0.152$ of the evolved-star sample reported by Grunblatt et al. (2018). This is not consistent with the trend in Grunblatt et al. (2018). As we discussed in Section 5.2, orbital decay happens when the orbital period is shorter than the stellar rotation period and thus may not happen in our targets. Perhaps this mismatch shows the systematic difference between the post-main-sequence evolution of systems with brown dwarf or low-mass star companions and hot Jupiters. However, there is currently a small sample of brown dwarfs (or planets) around evolved stars, and more detections are needed to reveal the detailed statistical properties of this population in comparison with the planetary population.

6 SUMMARY

In this paper, we confirmed one brown dwarf, TOI-2336b, and two objects near the hydrogen burning mass limit, TOI-1608b and TOI-2521b, transiting three aged stars. We analysed space and ground photometry as well as RVs from ground-based high-resolution spectra. TOI-2336b has a radius of $1.05 \pm 0.04\,R_J$, a mass of $69.9 \pm 2.3\,M_J$ and an orbital period of 7.71 days. TOI-1608b has a radius of $1.21 \pm 0.06\,R_J$, a mass of $90.7 \pm 3.7\,M_J$ and an orbital period of 2.47 d. TOI-2521b has a radius of $1.01 \pm 0.04\,R_J$, a mass of $77.5 \pm 3.3\,M_J$ and an orbital period of 5.56 d. Their host stars are F (TOI-2336, TOI-1608) and G (TOI-2521) type subgiant stars. In addition, we detected the secondary eclipse signal in the light curve of TOI-1608, while no signal was detected for TOI-2336 and TOI-2521. The corresponding constraints on the effective temperatures are 2983 ± 90 K for TOI-1608b, <3566 K for TOI-2336b, and <3143 K for TOI-2521b.

We found that all three companions have inflated radii via comparison to the evolution models for brown dwarfs and low-mass stars. Combining data from the literature, we fitted a relationship between radius, mass, and incident flux for brown dwarfs and low-mass stars, and we found that they are different between these two populations and also differ from the relationship of hot Jupiters. We found weak but statistically significant positive correlations between radius and flux for both brown dwarfs and low-mass stars, which indicates that these companions may also be inflated by the irradiation from host stars as hot Jupiters, though to a much lesser degree.

We analysed the tidal interactions in these three systems. We found that their relatively small eccentricities are consistent with their short orbital circularization time-scales. We also compared their stellar rotation periods and orbital periods and found that TOI-1608 and TOI-2521 are very likely to have reached spin-orbit synchronization. This phenomenon adequately explains the unusually rapid rotation of their host stars, which appear to be at odds with gyrochronology given their evolutionary stages. We examined the angular momentum distribution of these two systems following Hut (1981) and found that they can achieve and maintain stable spin-orbit synchronization. The estimated synchronization time-scales are also significantly shorter than their ages, further supporting the synchronization scenario. Additionally, we found a short orbital decay time-scale of 3.05 Myr

for TOI-1608, which may be detectable in future observations if it has not reached spin-orbit synchronization yet.

We compared the eccentricities of these three systems with previous statistical works. Compared with Ma & Ge (2014), they do not follow the trend that high-mass brown dwarf companions show more diversity in their eccentricity distribution than low-mass brown dwarf. Instead, they are consistent with the trend that companions with smaller periods tend to have lower eccentricities. This is in contrast with the hot Jupiter sample in Grunblatt et al. (2018), where short-period giant planets orbiting evolved stars tend to have larger eccentricities than the ones orbiting dwarfs. A larger sample of transiting brown dwarfs and low-mass stars will reveal more on the similarities and differences between these populations and the gas giant planets and provide more insights about their formation and evolution.

---

[8]http://www.astropy.org

This work makes use of observations from the LCOGT network. Part of the LCOGT telescope time was granted by NOIRLab through the Mid-Scale Innovations Program (MSIP). MSIP is funded by NSF. Resources supporting this work were provided by the NASA High-End Computing (HEC) Program through the NASA Advanced Supercomputing (NAS) Division at Ames Research Center for the production of the SPOC data products.

Some of the observations in this paper made use of the High-Resolution Imaging instrument Zorro and were obtained under Gemini LLP Proposal Number: GN/S-2021A-LP-105. Zorro was funded by the NASA Exoplanet Exploration Program and built at the NASA Ames Research Center by Steve B. Howell, Nic Scott, Elliott P. Horch, and Emmett Quigley. Zorro was mounted on the Gemini South telescope of the international Gemini Observatory, a programme of NSF's OIR Lab, which is managed by the Association of Universities for Research in Astronomy (AURA) under a cooperative agreement with the National Science Foundation. on behalf of the Gemini partnership: the National Science Foundation (United States), National Research Council (Canada), Agencia Nacional de Investigación y Desarrollo (Chile), Ministerio de Ciencia, Tecnología e Innovación (Argentina), Ministério da Ciência, Tecnologia, Inovações e Comunicações (Brazil), and Korea Astronomy and Space Science Institute (Republic of Korea).

DATA AVAILABILITY

This paper includes photometric data collected by the *TESS* mission and ground instruments, which are publicly available in ExoFOP, at https://exofop.ipac.caltech.edu/tess/target.php?id = 138017750 for TOI-1608, https://exofop.ipac.caltech.edu/tess/target.php?id = 88902249 for TOI-2336, and https://exofop.ipac.caltech.edu/tess/target.php?id = 72556406 for TOI-2521. All spectroscopy data underlying this article are listed in the appendix. All of the high-resolution speckle imaging data is available at the NASA exoplanet Archive with no proprietary period. The previous transiting BDs and low-mass stars sample and the codes for generating figures in Section 5 are available on https://github.com/Ssealevel/Codes_TOI-1608_2336_2521.

REFERENCES

Acton J. S. et al., 2021, MNRAS, 505, 2741
Albrecht S. et al., 2012, ApJ, 757, 18
Artigau É. et al., 2021, AJ, 162, 144
Astropy Collaboration, 2013, A&A, 558, A33
Astropy Collaboration, 2018, AJ, 156, 123
Astropy Collaboration, 2022, ApJ, 935, 167
Baraffe I., Chabrier G., Allard F., Hauschildt P. H., 2002, A&A, 382, 563
Baraffe I., Chabrier G., Barman T. S., Allard F., Hauschildt P. H., 2003, A&A, 402, 701
Baraffe I., Chabrier G., Barman T., 2008, A&A, 482, 315
Baraffe I., Homeier D., Allard F., Chabrier G., 2015, A&A, 577, A42
Barker A. J., Ogilvie G. I., 2009, MNRAS, 395, 2268
Beatty T. G., Morley C. V., Curtis J. L., Burrows A., Davenport J. R. A., Montet B. T., 2018, AJ, 156, 168
Benbakoura M., Réville V., Brun A. S., Le Poncin-Lafitte C., Mathis S., 2019, A&A, 621, A124
Bouchy F. et al., 2011, A&A, 525, A68
Brahm R., Jordán A., Espinoza N., 2017, PASP, 129, 034002
Brown T. M., Gilliland R. L., Noyes R. W., Ramsey L. W., 1991, ApJ, 368, 599
Brown T. M. et al., 2013, PASP, 125, 1031
Buchhave L. A. et al., 2010, ApJ, 720, 1118
Buchhave L. A. et al., 2012, Nature, 486, 375
Burrows A. et al., 1997, ApJ, 491, 856
Cañas C. I. et al., 2022, AJ, 163, 89
Caldwell D. A. et al., 2020, Res. Notes Am. Astron. Soc., 4, 201
Campante T. L. et al., 2016, ApJ, 830, 138
Carmichael T. W. et al., 2021, AJ, 161, 97
Carmichael T. W. et al., 2022, MNRAS, 514, 4944
Castelli F., Hubrig S., 2004, A&A, 425, 263
Chaplin W. J. et al., 2011, ApJ, 732, L5
Charbonneau D. et al., 2005, ApJ, 626, 523
Chen J., Kipping D., 2017, ApJ, 834, 17
Ciardi D. R., Beichman C. A., Horch E. P., Howell S. B., 2015, ApJ, 805, 16
Collier Cameron A. et al., 2007, MNRAS, 380, 1230
Collins K. A., Kielkopf J. F., Stassun K. G., Hessman F. V., 2017, AJ, 153, 77
Curtis J. et al., 2016, in 19th Cambridge Workshop on Cool Stars, Stellar Systems, and the Sun (CS19). Uppsala, Sweden, p. 95
Curtis J. L. et al., 2020, ApJ, 904, 140
Cutri R. M. et al., 2003, 2MASS All Sky Catalog of Point Sources. NASA/IPAC Infrared Science Archive
David T. J., Hillenbrand L. A., Gillen E., Cody A. M., Howell S. B., Isaacson H. T., Livingston J. H., 2019, ApJ, 872, 161
Donati J. F. et al., 2008, MNRAS, 385, 1179
Dotter A., 2016, ApJS, 222, 8
Espinoza N., 2018, Res. Notes Am. Astron. Soc., 2, 209
Espinoza N., Kossakowski D., Brahm R., 2019, MNRAS, 490, 2262
Fűrész G., 2008, PhD thesis, University of Szeged, Hungary
Findeisen K., Hillenbrand L., Soderblom D., 2011, AJ, 142, 23
Foreman-Mackey D., Hogg D. W., Lang D., Goodman J., 2013, PASP, 125, 306
Foreman-Mackey D., Agol E., Angus R., Ambikasaran S., 2017, AJ, 154, 220
Fulton B. J., Petigura E. A., Blunt S., Sinukoff E., 2018, PASP, 130, 044504
Furlan E., Howell S. B., 2017, AJ, 154, 66
Furlan E., Howell S. B., 2020, ApJ, 898, 47
Gaia Collaboration, 2016, A&A, 595, A1
Gaia Collaboration, 2021, A&A, 649, A1
Gill S. et al., 2022, MNRAS, 513, 1785
Giuricin G., Mardirossian F., Mezzetti M., 1984, A&A, 131, 152
Goldreich P., Soter S., 1966, Icarus, 5, 375
Grether D., Lineweaver C. H., 2006, ApJ, 640, 1051
Grieves N. et al., 2021, A&A, 652, A127
Grunblatt S. K. et al., 2016, AJ, 152, 185
Grunblatt S. K. et al., 2018, ApJ, 861, L5
Grunblatt S. K. et al., 2022, AJ, 163, 120
Henry T. J. et al., 2018, AJ, 155, 265
Howell S. B., Furlan E., 2022, Front Astron. Space Sci., 9, 871163
Howell S. B., Everett M. E., Sherry W., Horch E., Ciardi D. R., 2011, AJ, 142, 19
Howell S. B., Everett M. E., Horch E. P., Winters J. G., Hirsch L., Nusdeo D., Scott N. J., 2016, ApJ, 829, L2
Howell S. B., Scott N. J., Matson R. A., Everett M. E., Furlan E., Gnilka C. L., Ciardi D. R., Lester K. V., 2021, Front. Astron. Space Sci., 8, 10
Hut P., 1980, A&A, 92, 167
Hut P., 1981, A&A, 99, 126
Jackson B., Greenberg R., Barnes R., 2008, ApJ, 678, 1396
Jenkins J. M. et al., 2016, in Chiozzi G., Guzman J. C.eds, SPIE Conf. Ser. Vol. 9913, Software and Cyberinfrastructure for Astronomy IV. SPIE, Bellingham, p. 99133E
Jensen E., 2013, Astrophysics Source Code Library, record ascl:1306.007
Kipping D. M., 2013, MNRAS, 435, 2152
Kjeldsen H., Bedding T. R., 1995, A&A, 293, 87
Kreidberg L., 2015, Publ. Astron. Soc. Pac., 127, 1161
Kurucz R. L., 1992, in Barbuy B., Renzini A., eds, Proc. IAU Symp. 149, The Stellar Populations of Galaxies. Kluwer, Dordrecht, p. 225
Lester K. V. et al., 2021, AJ, 162, 75
Levato H., 1974, A&A, 35, 259
Li G., Winn J. N., 2016, ApJ, 818, 5

Li J., Tenenbaum P., Twicken J. D., Burke C. J., Jenkins J. M., Quintana E. V., Rowe J. F., Seader S. E., 2019, PASP, 131, 024506

Lightkurve Collaboration, 2018, Astrophysics Source Code Library, record ascl:1812.013

Lund M. N. et al., 2016, PASP, 128, 124204

Ma B., Ge J., 2014, MNRAS, 439, 2781

Maciejewski G. et al., 2016, A&A, 588, L6

Marcy G. W., Butler R. P., 2000, PASP, 112, 137

Marley M. S. et al., 2021, ApJ, 920, 85

Masuda K., Winn J. N., 2020, AJ, 159, 81

Matson R. A., Howell S. B., Horch E. P., Everett M. E., 2018, AJ, 156, 31

Matson R. A., Howell S. B., Ciardi D. R., 2019, AJ, 157, 211

Maxted P. F. L. et al., 2011, PASP, 123, 547

McLaughlin D. B., 1924, ApJ, 60, 22

Morton T. D., 2015, Astrophysics Source Code Library, record ascl:1503.010

Nakajima T., Oppenheimer B. R., Kulkarni S. R., Golimowski D. A., Matthews K., Durrance S. T., 1995, Nature, 378, 463

Nowak G. et al., 2017, AJ, 153, 131

Oppenheimer B. R., Kulkarni S. R., Matthews K., Nakajima T., 1995, Science, 270, 1478

Palle E. et al., 2021, A&A, 650, A55

Paredes L. A., Henry T. J., Quinn S. N., Gies D. R., Hinojosa-Goñi R., James H.-S., Jao W.-C., White R. J., 2021, AJ, 162, 176

Patra K. C., Winn J. N., Holman M. J., Yu L., Deming D., Dai F., 2017, AJ, 154, 4

Paunzen E., 2015, A&A, 580, A23

Pecaut M. J., Mamajek E. E., 2013, ApJS, 208, 9

Pecaut M. J., Mamajek E. E., Bubar E. J., 2012, ApJ, 746, 154

Pepe F. et al., 2002, Messenger, 110, 9

Persson C. M. et al., 2019, A&A, 628, A64

Phillips M. W. et al., 2020, A&A, 637, A38

Pollacco D. L. et al., 2006, PASP, 118, 1407

Psaridi A. et al., 2022, A&A, 664, A94

Queloz D. et al., 2001, Messenger, 105, 1

Rebolo R., Zapatero Osorio M. R., Martín E. L., 1995, Nature, 377, 129

Rebolo R., Martin E. L., Basri G., Marcy G. W., Zapatero-Osorio M. R., 1996, ApJ, 469, L53

Ricker G. R. et al., 2015, J. Astron. Telesc. Instr. Syst., 1, 014003

Rossiter R. A., 1924, ApJ, 60, 15

Saunders N. et al., 2022, AJ, 163, 53

Schlegel D. J., Finkbeiner D. P., Davis M., 1998, ApJ, 500, 525

Scott N. J. et al., 2021, Front. Astron. Space Sci., 8, 138

Siverd R. J. et al., 2018, in Evans C. J., Simard L., Takami H.eds, Proc. SPIE Conf. Ser. Vol. 10702, Ground-based and Airborne Instrumentation for Astronomy VII. SPIE, Bellingham, p. 107026C

Smith J. C. et al., 2012, PASP, 124, 1000

Spada F., Lanzafame A. C., 2020, A&A, 636, A76

Speagle J. S., 2020, MNRAS, 493, 3132

Spiegel D. S., Burrows A., Milsom J. A., 2011, ApJ, 727, 57

Stassun K. G., Torres G., 2016, AJ, 152, 180

Stassun K. G., Torres G., 2021, ApJ, 907, L33

Stassun K. G., Collins K. A., Gaudi B. S., 2017, AJ, 153, 136

Stassun K. G., Corsaro E., Pepper J. A., Gaudi B. S., 2018a, AJ, 155, 22

Stassun K. G. et al., 2018b, AJ, 156, 102

Stassun K. G. et al., 2019, AJ, 158, 138

Stumpe M. C. et al., 2012, PASP, 124, 985

Stumpe M. C., Smith J. C., Catanzarite J. H., Van Cleve J. E., Jenkins J. M., Twicken J. D., Girouard F. R., 2014, PASP, 126, 100

Tarter J. C., 1975, PhD thesis, University of California, Berkeley

Tayar J., Stassun K. G., Corsaro E., 2019, ApJ, 883, 195

Tokovinin A., 2018, PASP, 130, 035002

Tokovinin A., Fischer D. A., Bonati M., Giguere M. J., Moore P., Schwab C., Spronck J. F. P., Szymkowiak A., 2013, PASP, 125, 1336

Torres G., Andersen J., Giménez A., 2010, A&AR, 18, 67

Triaud A. H. M. J., 2018, in Deeg H. J., Belmonte J. A.eds, Handbook of Exoplanets. Springer International Publishing AG, part of Springer Nature, p. 2

Twicken J. D. et al., 2018, PASP, 130, 064502

Veras D., 2016, R. Soc. Open Sci., 3, 150571

Villaver E., Livio M., Mustill A. J., Siess L., 2014, ApJ, 794, 3

Weiss L. M. et al., 2013, ApJ, 768, 14

Wong I., Shporer A., Vissapragada S., Greklek-McKeon M., Knutson H. A., Winn J. N., Benneke B., 2022, AJ, 163, 175

Wright E. L. et al., 2010, AJ, 140, 1868

Yee S. W. et al., 2020, ApJ, 888, L5

Yu J., Huber D., Bedding T. R., Stello D., 2018, MNRAS, 480, L48

Zahn J. P., 1977, A&A, 57, 383

Ziegler C., Tokovinin A., Briceño C., Mang J., Law N., Mann A. W., 2020, AJ, 159, 19

APPENDIX A: THE POSTERIOR DISTRIBUTION OF ISOCHRONE FITTING FOR TOI-1608
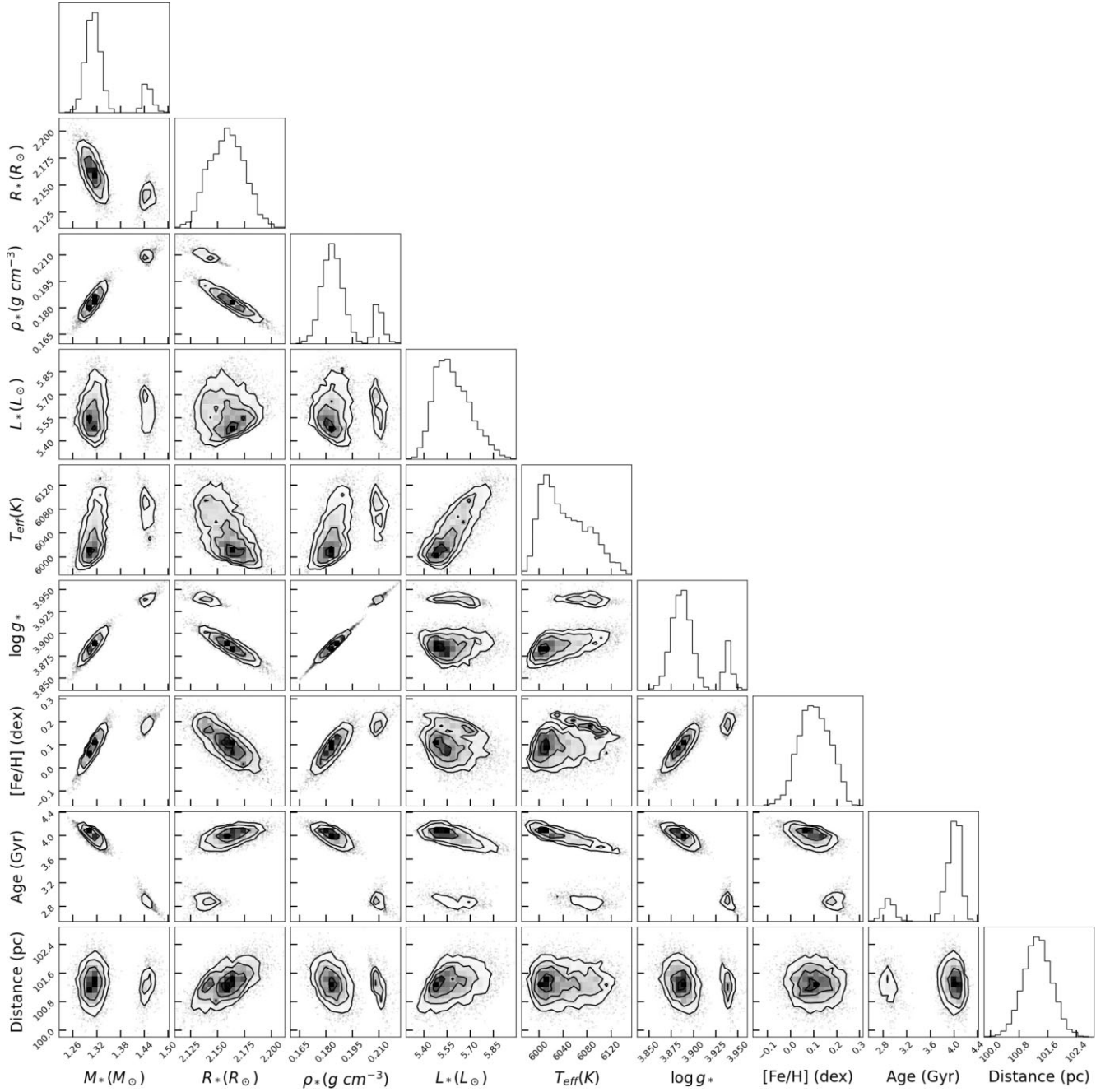
Figure A1. The posterior distribution of isochrone fitting for TOI-1608. The bimodal solution can be seen in the distribution of M_*, ρ_*, $\log g_*$, and age.

APPENDIX B: RV MEASUREMENTS

Table B1. RV measurements of TOI-1608.

BJD$_{TDB}$	RV (m s^{-1})	σ_{RV} (m s^{-1})	Instrument
2459551.809	77505.8	111.0	NRES
2459554.611	72125.0	115.4	NRES
2459555.828	92426.6	113.9	NRES
2459556.669	80122.9	117.2	NRES
2459569.599	72143.9	117.0	NRES
2459570.815	93377.1	136.1	NRES
2459571.662	74946.0	112.5	NRES
2459573.657	86689.7	317.6	NRES
2459574.790	74478.1	111.6	NRES
2459575.762	92945.6	119.0	NRES
2459586.564	74329.9	128.5	NRES
2459586.624	73127.7	135.1	NRES
2459586.691	72150.8	99.8	NRES
2459586.757	72454.5	140.4	NRES
2459588.610	84335.5	147.5	NRES
2459588.661	82298.2	101.6	NRES

Table B2. RV measurements of TOI-2336.

BJD$_{TDB}$	RV (m s^{-1})	σ_{RV} (m s^{-1})	Instrument
2459327.48570	36031.7	146.3	NRES
2459328.38208	33814.8	130.3	NRES
2459329.55779	25601.2	205.3	NRES
2459336.62242	34946.6	169.7	NRES
2459341.32044	39963.4	127.5	NRES
2459343.48120	35564.8	113.3	NRES
2459344.56582	30027.7	129.6	NRES
2459346.54750	30188.4	132.2	NRES
2459347.49433	34602.6	102.0	NRES
2459348.57917	37950.9	112.0	NRES
2459371.34618	36932.0	97.0	NRES
2459376.46575	29548.0	119.3	NRES
2459377.29886	31467.1	142.8	NRES
2459379.50367	38767.5	134.0	NRES
2459406.40547	28286.2	134.2	NRES
2459407.41335	26729.2	134.1	NRES
2459410.41467	38226.1	132.9	NRES
2459411.40852	37089.3	110.6	NRES
2459412.37610	35113.3	128.6	NRES
2459414.22659	28683.6	113.1	NRES
2459415.38816	27329.2	113.1	NRES

Table B2 – *continued*

BJD$_{TDB}$	RV (m s^{-1})	σ_{RV} (m s^{-1})	Instrument
2459342.68168	34035	219	CHIRON
2459345.72623	24826	164	CHIRON
2459349.70953	35637	180	CHIRON
2459357.62661	35468	206	CHIRON
2459359.65638	27702	198	CHIRON
2459371.64418	34388	128	CHIRON
2459387.65515	35618	178	CHIRON
2459399.56554	24837	215	CHIRON
2459407.61081	24916	186	CHIRON
2459417.57493	33182	191	CHIRON
2459424.53740	30008	214	CHIRON
2459432.50942	31233	205	CHIRON
2459318.877767	37598.76	121.12	CORALIE
2459321.804744	27564.77	111.03	CORALIE
2459328.784617	29880.55	119.24	CORALIE
2459331.872147	31218.65	99.95	CORALIE
2459335.705030	33463.34	109.05	CORALIE
2459343.687687	32204.50	125.93	CORALIE
2459346.774496	29472.14	99.30	CORALIE
2459351.752823	30681.14	120.70	CORALIE
2459356.753344	37656.42	123.56	CORALIE
2459357.723789	37554.35	77.79	CORALIE
2459358.643619	34352.13	99.49	CORALIE
2459361.597369	27438.35	65.13	CORALIE
2459363.736155	36053.07	107.73	CORALIE
2459365.700203	36685.84	69.86	CORALIE
2459368.608494	27031.54	78.39	CORALIE
2459373.599021	35976.49	64.58	CORALIE

Table B3. RV measurements of TOI-2521.

BJD$_{TDB}$	RV (m s^{-1})	σ_{RV} (m s^{-1})	Instrument
2459294.52983	−36161	53	CHIRON
2459295.53896	−40116	87	CHIRON
2459296.53688	−33715	53	CHIRON
2459297.55627	−24716	49	CHIRON
2459298.51469	−23135	112	CHIRON
2459301.52687	−38223	97	CHIRON
2459303.52923	−22904	66	CHIRON
2459304.50997	−25694	86	CHIRON

¹*Department of Astronomy, Tsinghua University, Beijing 100084, China*

²*Department of Physics and Kavli Institute for Astrophysics and Space Research, Massachusetts Institute of Technology, Cambridge, MA 02139, USA*

³*Departamento de Matemática y Física Aplicadas, Facultad de Ingeniería, Universidad Católica de la Santísima Concepción, Alonso de Rivera 2850, Concepción, Chile*

⁴*Centre for Astrophysics, University of Southern Queensland, West Street, Toowoomba, QLD 4350, Australia*

⁵*Observatoire de Genéve, Université de Genéve, Chemin Pegasi, 51,1290 Versoix, Switzerland*

⁶*Center for Astrophysics | Harvard & Smithsonian, 60 Garden Street, Cambridge, MA 02138, USA*

⁷*National Astronomical Observatories, Chinese Academy of Sciences, 20A Datun Road, Chaoyang District, Beijing 100012, China*

⁸*Department of Physics and Astronomy, Vanderbilt University, Nashville, TN 37235, USA*

⁹*Astrophysics Group, Keele University, Staffordshire ST5 5BG, UK*

¹⁰*NASA Ames Research Center, Moffett Field, CA 94035, USA*

¹¹*Department of Physics, Engineering and Astronomy, Stephen F. Austin State University, 1936 North St, Nacogdoches, TX 75962, USA*

¹²*SETI Institute, Mountain View, CA 94043, USA*

¹³*Jet Propulsion Laboratory, California Institute of Technology, Pasadena, CA 91109 USA*

¹⁴*NASA Exoplanet Science Institute, IPAC, California Institute of Technology, Pasadena, CA 91125 USA*

¹⁵*Center for Astrophysics | Harvard & Smithsonian, 60 Garden Street, Cambridge, MA 02138, USA*

¹⁶*Department of Astronomy, Columbia University, 550 West 120th Street, New York, NY, USA*

¹⁷*Department of Astrophysics, American Museum of Natural History, Central Park West at 79th Street, New York, NY 10024, USA*

¹⁸*Department of Physics and Astronomy, Johns Hopkins University, 3400 N Charles Street, Baltimore, MD 21218, USA*

¹⁹*Department of Astronomy, The Ohio State University, 4055 McPherson Laboratory, 140 West 18th Avenue, Columbus, OH 43210 USA*

²⁰*Department of Physics and Astronomy, The University of North Carolina at Chapel Hill, Chapel Hill, NC 27599-3255, USA*

²¹*Bay Area Environmental Research Institute, Moffett Field, CA 94035, USA*

²²*NASA Exoplanet Science Institute, Caltech/IPAC, Mail Code 100-22,1200 E. California Blvd., Pasadena, CA 91125, USA*

²³*Stellar Astrophysics Centre, Department of Physics and Astronomy, Aarhus University, Ny Munkegade 120, DK-8000 Aarhus C, Denmark*

²⁴*Proto-Logic LLC, 1718 Euclid Street NW, Washington, DC 20009, USA*

²⁵*Harvard-Smithsonian Center for Astrophysics, 60 Garden Street, Cambridge, MA 02138, USA*

²⁶*NASA Goddard Space Flight Center, 8800 Greenbelt Road, Greenbelt, MD 20771, USA*

²⁷*Department of Earth, Atmospheric, and Planetary Sciences, Massachusetts Institute of Technology, Cambridge, MA 02139, USA*

²⁸*Department of Aeronautics and Astronautics, Massachusetts Institute of Technology, Cambridge, MA 02139, USA*

²⁹*Kotizarovci Observatory, Sarsoni 90, 51216 Viskovo, Croatia*

³⁰*Planetary Discoveries in Fredericksburg, VA 22405, USA*

³¹*Department of Astrophysical Sciences, Princeton University, Princeton, NJ 08544, USA*

³²*Max Planck Institute for Solar System Research, Justus-von-Liebig-Weg 3, D-37077 Gottingen, Germany*

This paper has been typeset from a TEX/LATEX file prepared by the author.